A generic framework for evaluating the oceanic mixed layer depth dynamics

Alexandre Legay[1], Bruno Deremble[2], Thierry Penduff[3], Pierre Brasseur[4], and Jean-Marc Molines[4]

[1]Institut des Géosciences de l'Environnement
[2]Universite Grenoble Alpes
[3]Laboratoire de Glaciologie et Geophysique de l'Environnement, CNRS
[4]French National Centre for Scientific Research (CNRS)

January 15, 2024

A framework for evaluating ocean mixed layer depth evolution

Alexandre Legay[1], Bruno Deremble[1], Thierry Penduff[1], Pierre Brasseur[1], Jean-Marc Molines[1]

[1]Univ. Grenoble Alpes, CNRS, INRAE, IRD, Grenoble INP, IGE, 38000 Grenoble, France

Key Points:

- A parameter space is proposed to assess the evolution of the mixed layer depth for realistic forcings and preconditioning conditions
- The predictive skill of the parameter space is evaluated with a collection of 1D simulations
- Two applications demonstrate the utility of the parameter space, when used with realistic 3D ocean simulations

Corresponding author: Alexandre Legay, `alexandre.legay@univ-grenoble-alpes.fr`

Abstract

The mixed layer plays a crucial role as an entry or exit point for heat, salt, momentum, and nutrients from the surface to the deep ocean. In this study, we introduce a framework to assess the evolution of the mixed layer depth (MLD) for realistic forcings and preconditioning conditions. Our approach involves a physically-based parameter space defined by three dimensionless numbers: λ_s representing the relative contribution of the buoyancy flux and the wind stress at the air-sea interface, R_h the Richardson number which characterizes the stability of the water column relative to the wind shear, and f/N_h which characterizes the importance of the Earth's rotation (ratio of the Coriolis frequency f and the pycnocline stratification N_h). Four MLD evolution regimes ("restratification", "stable", "deepening" and "strong deepening") are defined based on the values of the normalized temporal evolution of the MLD. We evaluate the 3D parameter space in the context of 1D simulations and we find that considering only the two dimensions (λ_s, R_h) is the best choice of 2D projection of this 3D parameter space. We then focus on this two-dimensional λ_s - R_h parameter space and we present how this framework can be used to analyze 3D realistic ocean simulations. We discuss the impact of the horizontal resolution (1°, 1/12°, or 1/60°) and the Gent-McWilliams parameterization on MLD evolution regimes.

Plain Language Summary

Vertical mixing of water in the ocean occurs when cold air temperatures create dense cold water at the surface that tends to sink in the ocean or when a strong wind induces turbulence at the ocean surface. These processes mix heat and salt and create a layer at the top of the ocean that has a uniform temperature and salinity and that is called the "mixed layer". This mixed layer plays a fundamental role in the Earth climate system, and the representation of its evolution in ocean models hence needs to be assessed. For this purpose, we propose to map the mixed layer evolution in a three-dimensional space where the first axis is related to the wind and the surface heat flux, the second axis to the stability of the water column, and the third axis to the Earth's rotation. We show that this tool performs well statistically and we present how to use it in the context of realistic ocean models.

1 Introduction

The evolution of the mixed layer near the air-sea interface is primarily driven by the vertical mixing and restratification processes. Vertical mixing is usually driven by winds, surface cooling, brine rejection, Langmuir turbulence, and wave breaking (Marshall & Schott, 1999; Q. Li et al., 2019; Vreugdenhil & Gayen, 2021). In contrast, restratification processes are driven by solar heating, freshwater flux, or lateral processes such as mixed layer instabilities (see for example Boccaletti et al., 2007; Fox-Kemper et al., 2007). Accurately representing the mixed layer depth (MLD) evolution is crucial for capturing many physical and biogeochemical mechanisms, such as the sequestration of heat and carbon by the ocean (e.g. Banks & Gregory, 2006; Bernardello et al., 2014), the dynamics of marine ecosystems (e.g. Sverdrup, 1953; Lévy et al., 1998; Taylor & Ferrari, 2011), and the representation of the Atlantic meridional overturning circulation (e.g. Kuhlbrodt et al., 2007).

Historically, various approaches have been proposed to describe the evolution of the MLD which can be categorized into three main categories: bulk mixed layer models, similarity models, and turbulence closure models. For bulk mixed layer models, the governing equations of fluid dynamics are integrated over the mixed layer and represent the evolution of integrated properties (e.g. Kraus & Turner, 1967; Pollard et al., 1973; Price et al., 1986; Gaspar, 1988). These models have been used to derive theoretical scalings for the evolution of the MLD, such as the wind-driven deepening $h \propto u_* \, N^{-1/2} \, t^{1/2}$ (Pollard et al., 1973), observed empirically by Price (1979), and the free convection scaling $h \propto Q^{1/2} \, N^{-1} \, t^{1/2}$ (Turner, 1973; Van Roekel et al., 2018) measured empirically by Souza et al. (2020) (h being the MLD, u_* the surface friction velocity, t the time, Q the net surface heat flux and N the Brunt Väisälä frequency).

The second class of models are the similarity models such as the K-Profile Parameterization (KPP, Large et al., 1994) or the OSMOSIS model (Damerell et al., 2020; Madec et al., 2022). These models assume that the vertical profiles of tracers and momentum are self-similar. With this self-similarity hypothesis, turbulent fluxes can be computed by scaling a predefined profile shape with the magnitude of the surface forcing. Although the KPP model successfully captures many observed features of the ocean's boundary layer, it relies on empirical relationships and is not derived from first principles. Nev-

ertheless, KPP remains one of the most widely used parameterizations of convection in ocean models (Van Roekel et al., 2018; Q. Li et al., 2019; Souza et al., 2020).

The last class of models consists of the turbulence closure models. These models consider equations of higher order moments of the turbulent quantities and make some assumptions about their formulations in order to close the problem (e.g. Mellor, 1973; Mellor & Yamada, 1974, 1982). Widely used models in this class include the Turbulent Kinetic Energy (TKE) models, which solve a prognostic equation for TKE (Gaspar et al., 1990), and the Generic Length Scale (GLS) models which include an additional prognostic equation for the mixing length l (global description: Umlauf and Burchard (2003, 2005); examples of models of this type: $k-\epsilon$: Hanjalić and Launder (1972); Rodi (1987), $k - kl$: Mellor and Yamada (1982), $k - \omega$: Wilcox (1988), $k - \tau$: Zeierman and Wolfshtein (1986); Thangam et al. (1992)). Some models do not fit into one of the three aforementioned classes, such as the energetics-based Planetary Boundary Layer scheme (ePBL, Reichl & Hallberg, 2018), which combines a depth-dependent bulk mixed layer model with a turbulence closure model.

Currently, most climate simulations either use TKE or KPP models for vertical mixing (Zhu et al., 2020). The MLD evolution of these climate simulations depends on (i) the choice of vertical mixing scheme, (ii) the impact of resolved lateral processes, and (iii) as parameterizations for unresolved lateral effects (e.g. the Fox-Kemper et al. (2007) and the Gent and McWilliams (1990) parameterizations). Consequently, objectively comparing the MLD evolution in these climate simulations is challenging (Treguier et al., 2023). Common approaches involve comparing hydrographic sections at specific locations (e.g. evaluation at the Papa station: Gaspar et al., 1990; Large et al., 1994; Burchard & Bolding, 2001; Giordani et al., 2020), and/or conducting intercomparisons at specific times (e.g. with intercomparisons of MLD maps: Gutjahr et al., 2021; Heuzé, 2017), and/or using indirect metrics of the MLD evolution (e.g. by comparing the amount of deep water formed: Koenigk et al., 2021). However, these approaches only explore a limited range of forcings and preconditioning conditions.

In this paper, we adopt a more comprehensive approach by considering all possible ranges of forcings and preconditioning conditions in a suitable parameter space. Belcher et al. (2012) and Q. Li et al. (2019) have pioneered this approach to evaluate the representation of Langmuir circulation in different vertical mixing schemes. They proposed

a two-dimensional parameter space, with the first dimension (*i.e.* the first dimensionless number) assessing the relative importance of the wind and the wave forcings, and the second dimension characterizing the relative importance of wave and buoyancy forcings. In this parameter space, Belcher et al. (2012) and Q. Li et al. (2019) defined theoretical boundaries to highlight the importance of different surface forcings. Subsequently, Large eddy simulations (LES) carried out in the literature were placed in this parameter space to see which regimes are explored by these simulations. Their objective was to identify a potential bias arising from miscalibration of the LES simulations used to establish parameterizations.

Following the approach of Q. Li et al. (2019), our objective is to propose a dedicated parameter space to describe the evolution of the MLD. This parameter space aims to capture the MLD evolution dependency on the relative importance of wind and buoyancy forcings, preconditioning conditions (Marshall & Schott, 1999), and the influence of Earth's rotation. More precisely, we will evaluate the relative deepening or shoaling of the MLD over a 1-day period ($\partial_t h/h$ from noon to noon expressed in %/day). To keep the practicability of having few parameters, we have decided to exclude several processes (such as waves). Our study demonstrates that, at first order, three dimensionless numbers are enough for characterizing MLD evolution. In contrast to Q. Li et al. (2019), our approach involves directly plotting the values of MLD evolution $\partial_t h/h$ in the parameter space. This direct visualization allows for a more straightforward comparison of the behavior of different simulations.

This article is constructed as follows. First, we present in section 2 the three dimensionless numbers that constitute the parameter space. Secondly, we show in section 3.1 that MLD evolution regimes naturally emerge in this parameter space in the context of 1D simulations. Thirdly, we present in section 3.2 and section 3.3 two applications for showing how the parameter space can be used in practice with 3D realistic ocean models. The first application is about the impact of the lateral resolution on the MLD evolution regimes. The second one focuses on the effect of the Gent McWilliams parameterization which aims at representing the impact of the unresolved mesoscale processes in a coarse-resolution ocean model. Finally, we conclude in section 4 on the practical use of this three-dimensional parameter space and discuss its strengths and limitations.

2 Materials and Methods

2.1 Definition of the Three Dimensionless Numbers

We will formulate three dimensionless numbers to characterize the evolution of the mixed layer depth h of a 1D water column model that evolves from one day to another according to daily-mean surface forcings and preconditioning conditions. The goal here is to identify the main factors that drive the MLD evolution $\partial_t h$ in order to build a parameter space with a small number of dimensions being usable for evaluating $\partial_t h$. The principal omissions resulting from our choices will be discussed further in section 2.2.

We adopt the description of the water column given by bulk mixed layer models (e.g. Pollard et al., 1973): near the surface, we consider a well-mixed layer of thickness h. This layer is forced at the surface by the wind stress with a friction velocity $u_* = [(\overline{u'w'}|_{z=0})^2 + (\overline{v'w'}|_{z=0})^2]^{1/4}$ and the downward surface buoyancy flux $B_0 = -\overline{w'b'}|_{z=0}$ ($B_0 < 0$ for a destabilizing flux at the ocean surface), with u', v' and w' the turbulent velocities, the overline that denotes an average over small scale fluctuations (see Stull, 1988), b' the fluctuation of the buoyancy $b = -\frac{\rho - \rho_0}{\rho_0} g$, ρ the density, ρ_0 the reference density, and g the acceleration due to gravity. At the base of the mixed layer, the stratification is given by the Brunt Vaisala frequency N_h, which is sometimes called "preconditioning". In order to describe the MLD evolution, we have also opted to retain the local Coriolis parameter f. With this idealized view of the mixed layer, the MLD evolution $\partial_t h$ is a function of five physical quantities: (u_*, B_0, h, N_h, f). These 5 physical quantities are expressed with 2 distinct dimensions: length and time ($[u_*] = L.T^{-1}$, $[B_0] = L^2.T^{-3}$, $[h] = L$, $[N_h] = T^{-1}$, $[f] = T^{-1}$). The Vaschy-Buckingham theorem (π theorem) thus states that these five physical quantities can be represented by $5 - 2 = 3$ dimensionless numbers. The three dimensionless numbers we have chosen are

$$\lambda_s = \frac{-B_0 h}{u_*^3}, \tag{1}$$

$$R_h = \left(\frac{N_h h}{u_*}\right)^2, \tag{2}$$

and

$$f/N_h. \tag{3}$$

162 Note that λ_s is positive for a destabilizing surface buoyancy flux ($B_0 < 0$) and nega-

163 tive for a stabilizing surface buoyancy flux ($B_0 > 0$).

164 Henceforth, we describe the physical interpretations of these three dimensionless

165 numbers and then present the associated three-dimensional parameter space.

2.1.1 Physical Interpretation of λ_s

167 In the context of ocean mixed layer dynamics, λ_s can be interpreted in at least three

168 ways.

169 *1st Interpretation:* λ_s can be interpreted using the evolution equation of the Tur-

170 bulent Kinetic Energy (TKE; for a full description of this equation, see Hanjalić & Laun-

171 der, 1972; Rodi, 1987; Umlauf & Burchard, 2003):

$$\frac{Dk}{Dt} = P + G - \epsilon + \mathscr{D}_k \tag{4}$$

172 with $k = \frac{1}{2}(\overline{u'^2} + \overline{v'^2} + \overline{w'^2})$ the TKE, $P = -\overline{u'w'}\,\partial_z\overline{u} - \overline{v'w'}\partial_z\overline{v}$ the TKE produc-

173 tion by the shear (by conversion of mean kinetic energy), $G = \overline{w'b'}$ the TKE produc-

174 tion (or destruction) by the turbulent buoyancy flux (by conversion of mean potential

175 energy), ϵ the TKE dissipation, and $\mathscr{D}_k$ the TKE diffusion.

176 The surface layer is defined as the zone where the turbulent fluxes vary by less than

177 $10\,\%$ from their values at $z = 0$ (Stull, 1988). In this zone, we can consider $\overline{u'w'} \approx \overline{u'w'}|_{z=0} \propto$

178 u_*^2 and $G \approx \overline{w'b'}|_{z=0} = -B_0$. Since the surface mean horizontal velocity $\overline{u}|_{z=0}$ is well

179 correlated to the surface friction velocity u_* (Weber, 1983), and if we neglect the mean

180 horizontal velocity $\overline{u}$ below the mixed layer depth (Pollard et al., 1973), then an order

181 of magnitude of $\partial_z\overline{u}$ is given by u_*/h. It follows $P \propto u_*^3/h$. An evaluation of G/P in

182 the surface layer finally gives

$$\left.\frac{G}{P}\right|_{surf} \propto \frac{-B_0}{\left(\frac{u_*^3}{h}\right)} \equiv \lambda_s. \tag{5}$$

183 This ratio $G/P\,|_{surf}$ is by definition the flux Richardson number R_f evaluated in

184 the surface layer (Mellor & Durbin, 1975). It gives the relative contribution of surface

185 buoyancy flux and wind for the production of TKE. In the case $B_0 < 0$ *i.e.* $G/P\,|_{surf} >$

186 0, both terms produce TKE. On the other hand, in the case of a restratifying buoyancy

flux $B_0 > 0$, there is a competition between production by the shear ($P > 0$) and destruction by the turbulent buoyancy flux ($G < 0$). Particularly, for $G/P|_{surf} < -1$, more TKE is destroyed (converted into mean potential energy) than created (from mean kinetic energy): this likely represents a restratification event.

2nd Interpretation: We can also interpret λ_s in the light of the Monin-Obukhov similarity theory (Obukhov, 1971). This theory, which is valid in the surface layer, introduces the Monin-Obukhov length L_{MO}:

$$L_{MO} = \frac{u_*^3}{\kappa B_0}. \tag{6}$$

We give here its definition in the oceanic framework (see for example Zheng et al., 2021) which is the opposite of the atmospheric definition. The physical interpretation of L_{MO} was introduced by Obukhov in the case $L_{MO} < 0$ ($\Leftrightarrow B_0 < 0 \Leftrightarrow \lambda_s > 0$). In this regime, L_{MO} estimates the typical thickness of a "sub-layer of dynamic turbulence" in which stratification is of little importance and the turbulence dynamics is governed by the mean-current shear (Obukhov, 1971), *i.e.* the production of TKE by the buoyancy G is negligible in comparison to the one by the mean-current shear P. In practice, Wyngaard (1973) has shown that $G \simeq P$ for $z \simeq 0.5 L_{MO}$ (Fig 5.22 Stull, 1988). The number λ_s can be seen as

$$\lambda_s = \frac{1}{\kappa} \frac{-h}{L_{MO}}. \tag{7}$$

Thus, $\lambda_s < 0.5/\kappa$ gives $P > G$ in the mixed layer while $\lambda_s > 0.5/\kappa$ means $G > P$. It is important to recall that this interpretation only stands for $L_{MO} < 0$ ($\Leftrightarrow B_0 < 0 \Leftrightarrow \lambda_s > 0$). For the case $L_{MO} > 0$ ($\Leftrightarrow B_0 > 0 \Leftrightarrow \lambda_s < 0$), we refer to our first interpretation of λ_s.

3rd Interpretation: In the case $B_0 < 0$, convective thermals have a velocity in the order of $w_* = (-B_0 h)^{1/3}$ (Willis & Deardorff, 1974; Marshall & Schott, 1999). Then λ_s can be written as

$$\lambda_s = \left(\frac{w_*}{u_*}\right)^3. \tag{8}$$

210   In this expression, it is clear that λ_s measures the relative importance of mechan-
211   ical and convective forcings.

212   Last, it is worth noting that in a different context Simpson and Hunter (1974) used
213   a similar ratio to characterize the mixing occurring in the Irish Sea where u_* was related
214   to the tidal forcing (friction in the bottom boundary layer).

2.1.2 Physical Interpretation of R_h

216   The dimensionless number R_h can be interpreted as a Richardson number. By def-
217   inition the gradient Richardson number $Ri = N^2/(\partial_z \overline{u})^2$ is the ratio of the stabilizing
218   effect of the stratification and the destabilizing effect of the shear of the mean current
219   (see for example Mack & Schoeberlein, 2004). We compare here the stratification at the
220   mixed layer base N_h^2 with the order of magnitude of the wind-induced shear u_*/h. This
221   gives the ratio:

$$\frac{N_h^2}{(\frac{u_*}{h})^2} \equiv R_h. \tag{9}$$

222   We could have included the contribution of w_* to the shear but we will see in sec-
223   tion 2.3 that this omission is intentional and results in a simpler interpretation of the
224   parameter space.

2.1.3 Physical Interpretation of f/N_h

226   In the context of mixed layer dynamics, there are several interpretations for the
227   dimensionless number f/N_h.

228   First, the ratio f/N_h can be seen as h/L_d, where $L_d \propto Nh/f$ is the "mixed layer"
229   Rossby radius of deformation in the quasi-geostrophic context (h is not the total depth
230   of the fluid but the mixed layer depth). In the situation where $f/N_h > O(1)$, we ex-
231   pect that mixed layer instabilities will create a lateral buoyancy flux (see Boccaletti et
232   al., 2007). Part of the turbulent energy normally used for vertical mixing is hence used
233   for lateral mixing. Therefore, we expect that values $f/N_h > O(1)$ result in a slowdown
234   of the MLD deepening. In the specific context of the free convection regime, rapid ro-
235   tation is also known to decrease the turbulent heat flux (see Bouillaut et al., 2019; Au-
236   rnou et al., 2020), and so we expect that for high values of f/N_h, we are likely to ob-

serve a reduced MLD deepening. Finally, one last possible interpretation of f/N_h was given by Speer and Marshall (1995) who have described how the aspect ratio of convective plumes is determined by the ratio f/N_h, where the effect of rotation is mainly to alter the lateral spreading of convective structures (see also Deremble, 2016).

2.2 Limitations

There are of course other physical phenomena that occur in the mixed layer and that we have not taken into account:

- The effect of waves and associated Langmuir turbulence that could have been represented through the values of the surface Stokes drift u_0^S (Q. Li et al., 2019). However, it is worth mentioning that part of u_0^S can be explained by u_*. Minimal parameterizations of Langmuir turbulence even define u_0^S directly proportional to u_* (M. Li & Garrett, 1993; Madec et al., 2022). Thus, some of the wave impacts are implicitly contained through the consideration of u_*.

- All the effects of the horizontal gradients (of velocities, pressure...) and advections that are present in a 3D realistic ocean model. We can particularly pinpoint the Ekman flow that can create an equivalent stabilizing/destabilizing wind-driven buoyancy flux (see for example Thomas & Lee, 2005), and the impacts of the restratification by baroclinic instability at convective fronts or at mesoscale eddy fronts. Some of these aspects can be captured by looking at the isopycnal slopes and this point will be further discussed in section 3.3.

- The influence of the vertical shear of the horizontal velocities. As we work with daily evolution, and knowing the Ekman theory (Ekman, 1905), we can expect this shear to be partly represented by the consideration of the surface wind friction velocity, the mixed layer depth, and the Coriolis parameter.

Considering many of these aspects would have meant adding more dimensions to the parameter space and thus reducing its practical use. We will see in the results that the dimensionless numbers we have chosen are in many situations sufficient to obtain a significant prediction of the MLD evolution and therefore capture well the dominant processes of this evolution.

2.3 Other Possible Dimensionless Numbers

We have defined three dimensionless numbers from the five physical quantities (u_*, B_0, h, N_h, f), but other choices could have been possible. We want to highlight here some of them:

- The Rossby number $Ro = u_*/(hf)$ that characterizes the relative importance of the inertial and the Coriolis forces (Van Der Laan et al., 2020).

- The ratio $h/h_{\max}$ with $h_{\max} = 2^{0.75} u_*/\sqrt{Nf}$ which compares the current h to the maximum one $h_{\max}$ predicted by Pollard et al. (1973) in case of a shear-driven MLD deepening in a rotating case. It is known that h does not really stop at $h_{\max}$ but this value represents an important threshold of the deepening (Ushijima & Yoshikawa, 2020).

- In case of $B_0 < 0$, the Richardson number $R_h^* = (N_h h/w_*)^2$ constructed with w_* rather than u_* which compares the stabilizing effect of the stratification and the destabilizing impact of the buoyancy flux (Turner, 1986; Shy, 1995). However, R_h^* can be expressed as

$$R_h^* = R_h/\lambda_s^{2/3} \tag{10}$$

and hence, in a log-log parameter space (λ_s, R_h), we will see that the isolines of R_h^* appear as lines of slope 2/3. Then, we have the possibility to see the isolines of both R_h and R_h^* at the same time in the parameter space. We will use this information to decide whether one or the other is more representative of the deepening situation. This would have been impossible if we had taken a Richardson number defined with the two contributions at the same time, such as $(N_h h/\sqrt{u_* w_*})^2$, $(N_h h/\max(u_*, w_*))^2$ or $(N_h h/(u_* + w_*))^2$.

The next four sections present the simulations we will use to evaluate the parameter space and to conduct the two model sensitivity studies. In the next three sections, we present three 3D realistic ocean simulations at three different horizontal resolutions (1/60°, 1/12°, and 1°). These simulations will be used to study the impact of the horizontal resolutions on the MLD evolution regimes. Table 1 summarizes the main features of these simulations.

2.4 NEMO-eNATL60 1/60° Basin-scale North Atlantic Ocean Simulation

The eNATL60-BLBT02 (eNATL60) simulation (Brodeau et al., 2020) is a basin-scale North Atlantic ocean/sea-ice simulation forced by the atmospheric 3-hourly ERA-Interim reanalysis (Dee et al., 2011) on a 1/60°-horizontal and 300-vertical-level grid. It includes an explicit tidal forcing. The lateral boundary conditions for the ocean velocities, temperature, and salinity are based on the GLORYS12 v1 reanalysis (Lellouche et al., 2021). Vertical mixing is governed by a Turbulent Kinetic Energy (TKE) scheme combined with the Enhanced Vertical Diffusivity (EVD) parameterization which increases the vertical diffusivity in case of unstable water columns (Lazar et al., 1999; Madec et al., 2022). The Fox-Kemper parameterization (Fox-Kemper et al., 2007), which represents the restratifying effect of sub-mesoscale mixed layer eddies, is included. The model outputs, ignoring the spin-up period, cover 10 months from 1 January 2010 to 29 October 2010. A description of the technical choices and the configuration files are available at `https://github.com/ocean-next/eNATL60`. For our study, we extracted daily averages of the data in two regions of interest (Figure 1). The "Western Mediterranean region" extends from 2 °E to 10 °E and from 40 °N to 44 °N, and the "Labrador region" from 56 °W to 51 °W and from 55 °N to 59 °N. To avoid shallow water coastal dynamics, we only kept locations for which the local depth is greater than or equal to 2000 m. Moreover, to reduce the amount of data, we subsampled the horizontal resolution of the outputs from 1/60° to 1/12°. For doing that, we used the function "samplegrid" of the Climate Data Operators library (CDO; Schulzweida, 2023) with a subsampling factor of 5 on both x and y dimensions of the grid.

2.5 NEMO ORCA 1/12° Global Ocean Simulation

The eORCA12.L75-GJM2020 (eORCA12) simulation is a global ocean/sea-ice simulation forced by the atmospheric reanalysis JRA55-do 1.4.0 (Tsujino et al., 2018) performed on the ORCA12.L75 grid (1/12° horizontal resolution and 75-level non-uniform vertical grid) over the period 1979-2019. Vertical mixing is governed by a TKE + EVD + IWM (additional parameterization accounting for mixing due to internal waves) scheme. A description of the technical choices and the configuration files are available at `https://github.com/meom-configurations/eORCA12.L75-GJM2020`. In this study, we used a 10-year period (1 January 2006 to 1 January 2015) and we extracted daily averages of

Table 1. Summary of the main features of the simulations. "Med" and "Lab" stand for respectively the "Western Mediterranean" and the "Labrador" extractions (see text)

Simulation	Horizontal resolution [[Subsampling]]		Total time		Vertical mixing scheme	Additional parameterization	Reference
	Med/Lab	Global	Med/Lab	Global			
eNATL60	1/60° [[1/12°]]	-	10 months (Jan to Oct 2010)		TKE + EVD	Fox-Kemper	Brodeau et al., 2010 (https://github.com/ocean-next/eNATL60)
eORCA12	1/12°	[[15°]]	10 years (2006 to 2015)		TKE + EVD	Internal Wave Mixing (IWM)	https://github.com/meom-con gurations/ eORCA12.L75-GJM2020
eORCA1	1°	[[15°]]	20 years (2000 to 2019)		TKE + EVD	-	https://github.com/meom-con gurations/ eORCA1-GJM2020
eORCA1GM	1°	[[15°]]	20 years (2000 to 2019)		TKE + EVD	Gent McWilliams (GM)	https://github.com/meom-con gurations/ eORCA1-GJM2020
Collection of 1D simulations	-		20 years (2006 to 2015)	10 years (2000 to 2019)	TKE + EVD	-	https://github.com/legaya/ James2023_ParameterSpace/

the data on the same Western Mediterranean and Labrador regions as described above (Figure 1), with the same restriction of keeping only locations for which the local depth is greater than or equal to 2000 m. Unlike eNATL60, which is not a global simulation, we are also going to use the results of eORCA12 at the global scale and, to reduce the amount of data, we subsampled the outputs from the 1/12° resolution to only keep 234 points placed on a 15° grid (cf Figure 1). This coarse representation is enough to capture a realistic range of f/N_h, representative of the world's oceans.

2.6 NEMO ORCA 1° Global Ocean Simulation

We performed the eORCA1-GJM2020 (eORCA1) simulation in a set-up that is the same as the eORCA12 simulation, except for the horizontal resolution. However, a 1° horizontal resolution is not considered eddy-resolving and for this reason, an eddy-induced velocity is often added at this resolution to parameterize missing mesoscale eddies. We computed this eddy-induced velocity with the Gent McWilliams (GM) parameterization (Gent & McWilliams, 1990). We performed two experiments, eORCA1 without GM and eORCA1GM with GM. The GM coefficient was taken constant (with the NEMO default input parameters of lateral diffusive velocity Le = $0.02\,\mathrm{m\,s^{-1}}$ and lateral diffusive velocity Ue = $2 \times 10^5\,\mathrm{m}$). A description of the technical choices and the configuration files are available at `https://github.com/meom-configurations/eORCA1-GJM2020`. We took daily averages of the outputs over 20 years from 1 January 2000 to 1 January 2019. We extracted the outputs on the two regions of interest, as well as at the global scale sub-
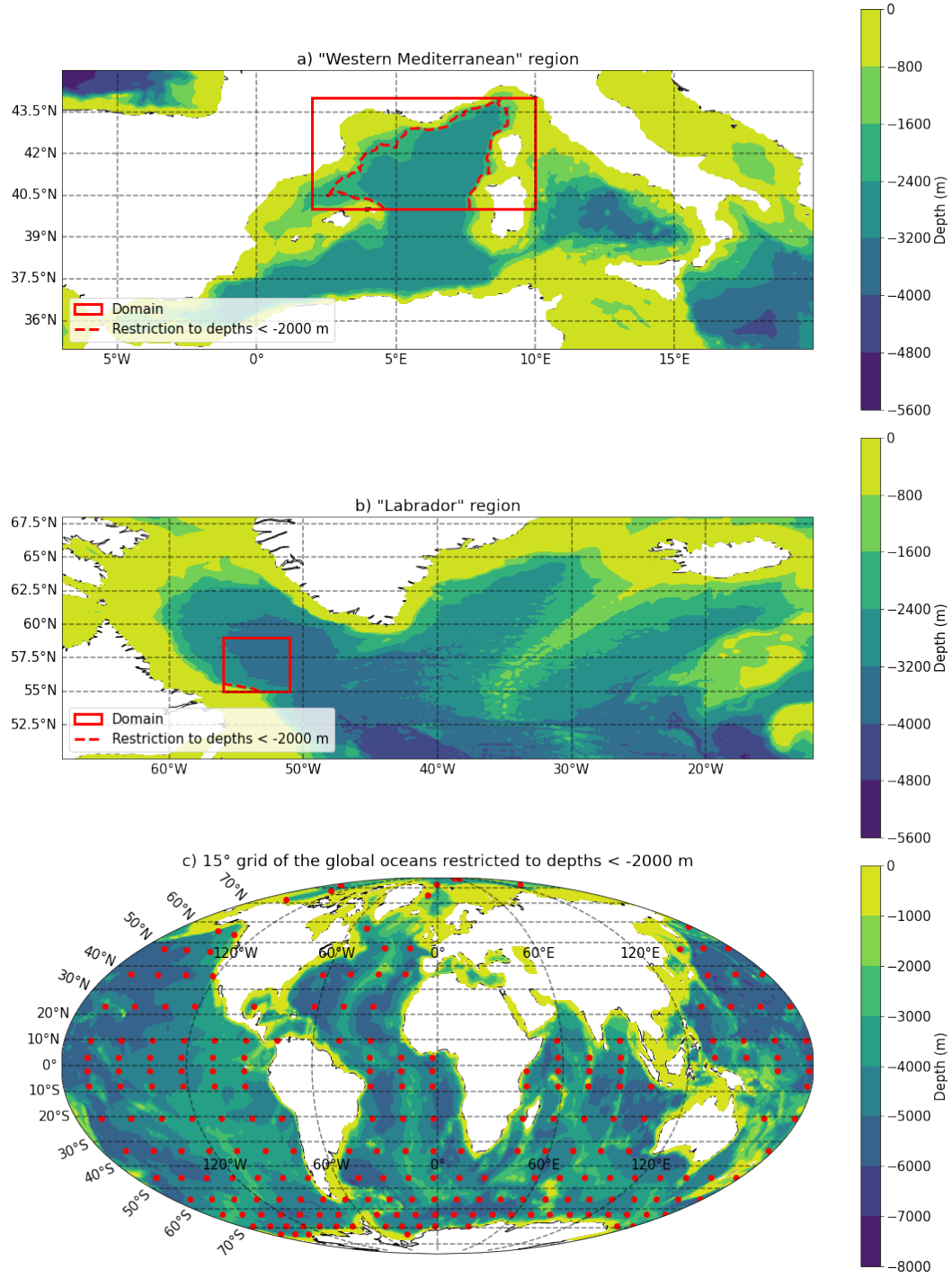
Figure 1. The three regions of interest in this study. a) and b) are respectively the "Western Mediterranean" region that extends from 2 °E to 10 °E and from 40 °N to 44 °N, and the "Labrador" region that extends from 56 °W to 51 °W and from 55 °N to 59 °N. c) presents the 15° grid used at the global scale (Mollweide's projection). All of these three regions are restricted to depths greater than 2000 m.

344 sampled on the 15° grid described in the previous section. Again, only the locations for

345 which the local depth is greater than or equal to 2000 m were kept.

2.7 1D Simulations

347 This section presents the 1D simulations we will use to classify the MLD evolution

348 regimes in the parameter space.

349 We performed a collection of 1D water column simulations using the code presented

350 in Fearon et al. (2020), which is a standalone 1D vertical version of the Coastal and Re-

351 gional Ocean COmmunity model (CROCO, `https://www.croco-ocean.org/`). This col-

352 lection contains 20-year simulations from 1 January 2000 to 1 January 2019 at all the

353 1° grid locations of the two regions Labrador and Western Mediterranean, as well as 10-

354 year simulation from 1 January 2006 to 1 January 2015 for all the points of the global

355 subsampled grid of 15° resolution. To be consistent with the 3D models, we used a TKE

356 + EVD scheme, we included the Earth's rotation, we kept only the locations where the

357 local depth is greater than 2000 m and we applied the same atmospherical forcings as

358 the eORCA1 simulation (presented in section 2.6). The wind, precipitation, evaporation,

359 and non-solar heat flux forcings were applied daily with 24-hour constant values. The

360 solar flux was constructed with a cosine truncated of its negative values, thus represent-

361 ing 12 h daytime with positive values and 12 h nighttime with zero values. The temper-

362 ature and salinity profiles were re-initialized to their eORCA1 values at the beginning

363 of each new year, so these simulations should be viewed as multiple annual simulations.

364 The vertical grid was taken equal to the one of eORCA1/eORCA12 cut at 2000 m depth,

365 hence the 54 shallowest levels of this 75-level grid. The time step was set to 360 s. The

366 UNESCO 1983 nonlinear equation of state was used (Fofonoff & Millard Jr, 1983). At

367 the bottom boundary of the domain, we imposed a homogeneous Neumann condition

368 (no flux).

2.8 Practical Calculation of the Dimensionless Numbers

370 The five physical quantities (u_*, B_0, h, N_h, f) appearing in the dimensionless num-

371 bers are calculated as follows:

372 • The surface wind friction velocity is calculated from its definition $u_* = \sqrt{|\tau^w|/\rho_0}$

373 with $|\tau^w|$ the norm of the wind stress vector at the ocean surface.

- We calculate the surface buoyancy flux with its classical linear definition: $B_0 = \frac{g}{\rho_0}\left(\frac{\alpha Q}{c_p} - \beta S_{surf}(E - P)\right)$ with Q the downward surface heat flux ($Q < 0$ for cooling), E the evaporation, P the precipitation, c_p the heat capacity per unit mass, S_{surf} the surface salinity, ρ_0 the reference density, and (α, β) respectively the thermal expansion coefficient and the haline contraction coefficient of the linearized equation of state $\rho = \rho_0(1 - \alpha(T - T_0) + \beta(S - S_0))$ with T_0 the reference temperature and S_0 the reference salinity. These two coefficients (α, β) are calculated for each location at every time step according to the local values of the surface temperature and the surface salinity.

- We choose the classical MLD definition of the CMIP6 working group for h (Griffies et al., 2016, Appendix H24.2). This definition is based on a buoyancy difference from the surface and was designed to give results similar to the density criterion of a $0.03\,\mathrm{kg/m^3}$ difference of de Boyer Montégut et al. (2004) in the case of a local density close to $1035\,\mathrm{kg/m^3}$.

- The stratification at the base of the mixed layer N_h^2 is defined as a difference between the properties at the MLD ($z = -h$) and $10\,\%$ below the MLD ($z = -1.1h$):

$$N_h^2 = \frac{g}{\rho_0}\frac{\rho(z = -1.1h) - \rho(z = -h)}{0.1h}. \tag{11}$$

  It is worth mentioning here that, if we interpret $\Delta\rho = \rho(z = -1.1h) - \rho(z = -h)$ as the "density jump" at the base of the mixed layer, $R_h = (N_h h/u_*)^2$ can be written as $R_h = g\frac{\Delta\rho}{\rho_0}h/(0.1u_*^2)$ and is hence proportional to $R_\tau = g\frac{\Delta\rho}{\rho_0}h/u_*^2$ the bulk Richardson number associated to the wind (Price, 1979).

- The Coriolis parameter is equal to $f = 2\Omega_0\sin(\phi)$ with $\Omega_0 = 7.29\times10^{-5}\,\mathrm{rad\,s^{-1}}$ the rotation rate of the Earth and ϕ the latitude. As we did not consider any lateral gradients, the sign of f is of course not important in our context and we thus consider the absolute value of f. However, throughout the manuscript, we write f rather than $|f|$ for brevity.

Sensibility of the results to other choices of MLD definitions (de Boyer Montégut et al., 2004; Reichl & Hallberg, 2018) and other N_h^2 evaluations (centered at $z = -h$ or with a constant distance of $15\,\mathrm{m}$ below the MLD, see the discussion in Sérazin et al., 2023) were tested but not shown here for brevity. In short, the two definitions we chose were the ones giving the results with the highest significance (the notion of "significance"

in the parameter space is defined in the next section) and hence the ones that are the more relevant in our context of the evaluation of the relative MLD deepening or shoaling over a 1-day period.

As we follow the MLD evolution over a 1-day period, we use the daily averages of the quantities (from noon to noon). We opt to take the daily averages of h and N_h^2 at day $d-1$, and u_* and B_0 at day d. The reason is that h and N_h^2 represent an initial state, with a MLD h in which thermals can develop underlying a stable stratification N_h^2. This initial state is modified by a whole day of forcing of u_* and B_0. Hence, the temporal evolutions of the MLD $\partial_t h$ are computed over this 1-day period (day $d-1$ to day d). Finally, we note that the calculation of $\Delta\rho = \rho(z = -1.1h) - \rho(z = -h)$, needed to obtain N_h^2 (see Equation 11), can present two problems. First, N_h^2 can be negative if there is an instability at the base of the mixed layer. These cases represent less than $0.01\,\%$ of the points and are simply discarded. Second, the calculation of $\Delta\rho$ is not defined if the mixed layer reaches the bottom of the domain. These points, which correspond to a zero $\partial_t h$ evolution, also represent less than $0.01\,\%$ of all cases and are discarded as well.

2.9 Visualization in the Parameter Space

We characterize the MLD evolution through the relative change of the MLD $\partial_t h/h$, expressed in %/day. This variable is not dimensionless and could have been normalized by dividing by a characteristic time t_c. Several possibilities were tested. However, since this change makes it more difficult to understand the variable, and since none of the trials produced any improvement in the results, none of the possibilities were retained.

The parameter space has three dimensions: λ_s, R_h, and f/N. For exploring these three dimensions, we use projections into two-dimensional parameter spaces λ_s - f/N, R_h - f/N, and λ_s - R_h. To facilitate the intercomparison of two graphs, we use hexagonal bin plots rather than scatter plots and we define four MLD evolution classes according to the value of $\partial_t h/h$. Comparing two graphs can then be done by looking at the MLD evolution class obtained hexagon by hexagon. The four MLD evolution regimes are defined as follows

- $\partial_t h/h \geq 10\,\%$/day: **Strong Deepening**

- $1\,\%$/day $\leq \partial_t h/h < 10\,\%$/day: **Deepening**

- $-1\,\%/\mathrm{day} \leq \partial_t h/h < 1\,\%/\mathrm{day}$: **Stable**

- $\partial_t h/h < -1\,\%/\mathrm{day}$: **Restratification**

The class of a hexagon is determined by the majority class of its constituent points. That is, for every hexagon of a 2D parameter space we sort all the points inside this hexagon in one of the 4 classes and the class of the hexagon is the one that is the most represented. If this class represents more than 75 % of the points, it is tagged as "highly significant". If this percentage is between 50 % and 75 %, it is tagged as "significant". If it is below 50 %, it is considered not significant. For statistical reasons, a hexagon is kept only if it contains at least 30 points.

3 Results

In this section, we populate the 3D parameter space (λ_s, R_h, f/N_h) with 1D simulations performed at the global scale and we show that considering only the two dimensions (λ_s, R_h) is the best choice of 2D projection of this 3D parameter space. We then focus on this two-dimensional λ_s - R_h parameter space and we present how this framework can be used to analyze 3D realistic ocean simulations. The first application is about the impact of the lateral resolution on the MLD evolution regimes. The second application focuses on the effect of the Gent McWilliams parameterization which aims at representing the impact of the unresolved mesoscale processes in a coarse-resolution ocean model.

3.1 Evaluation of the Three-Dimensional Parameter Space

The three-dimensional parameter space λ_s - R_h - f/N_h is evaluated with 1D simulations performed at the locations of the 15° global grid (described in section 2.7). We first show that the (λ_s, R_h) projection is the best choice of 2D projection of this 3D parameter space. We then highlight the influence f/N_h.

Figure 2 displays the three two-dimensional projections of the 3D parameter space λ_s - R_h - f/N_h. Among these three projections, the 2D parameter space λ_s - R_h exhibits the highest significance with the MLD evolution classes of its hexagons being significant in 96 % of the cases. In comparison, the significance is 84 % for the f/N_h - R_h projection and 73 % for the λ_s - f/N_h projection (definition of the "significance" in section 2.9).

Table 2. Significances of the MLD evolution classes of the hexagons for the three 2D projections of the 3D parameter space λ_s - R_h - f/N_h

2D parameter space	λ_s - R_h	f/N_h - R_h	λ_s - f/N_h
Highly significant hexagons	74 %	46 %	30 %
Significant hexagons	22 %	38 %	43 %
Not significant hexagons	4 %	16 %	27 %

Moreover, among these significant hexagons, the λ_s - R_h parameter space shows the highest number of highly significant hexagons: 74 % of all hexagons (46 % for f/N_h - R_h; 30 % for λ_s - f/N_h; cf Table 2).

In addition to the high significance levels, the λ_s - R_h projection also exhibits the best "spatial coherence": the four MLD evolution regimes are organized in well-delimited continuous zones. The main thresholds delineating these zones are plotted in Figure 2.a. and are as follows:

- **Vertical threshold at $\lambda_s = -3$:** Physically, we expect restratification for $G/P|_{surf} < -1$, indicating that the surface buoyancy flux removes more TKE than the amount produced by the wind. In terms of λ_s (that is $\propto G/P|_{surf}$), the threshold seems to be around $\lambda_s \approx -3$. The criterion $\lambda_s < -3$ corresponds to stable or restratification regimes and is consistent with a TKE-loss situation. This $\lambda_s < -3$ threshold is also observed in the λ_s - f/N_h parameter space and so does not depend on f/N_h.

- **Horizontal thresholds in the range $-3 < \lambda_s < 0$:** In the range $-3 < \lambda_s < 0$, the boundaries are horizontal, indicating that, when the wind dominates over the buoyancy flux, only the value of R_h is important for predicting the MLD evolution regime. A value of $R_h > 1000$ corresponds to "stable" regime, $1000 < R_h < 300$ corresponds to "deepening" regime and $R_h < 300$ corresponds to "strong deepening" regime. This progression according to R_h corresponds to the traditional interpretation of a Richardson number. For High values of R_h, the shear u_*/h is too weak to erode the pycnocline stratification N_h, leading to a stable regime. In contrast, low values of R_h result in MLD deepening regimes.
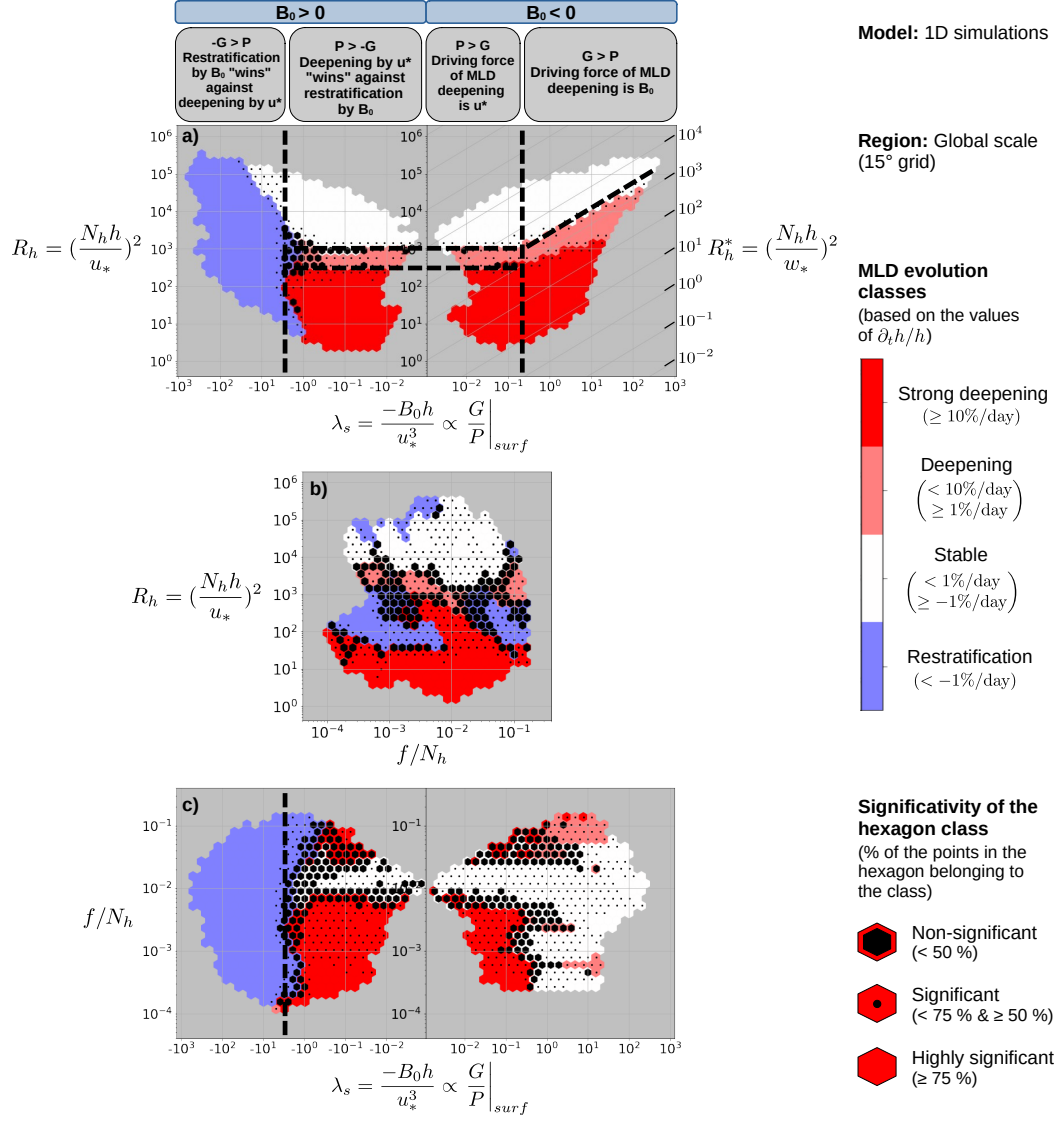
Figure 2. Results of the 1D simulations performed at the locations of the 15° global grid, plotted in the three different 2D projections of the 3D parameter space: (a) λ_s - R_h, (b) f/N_h - R_h and (c) λ_s - f/N_h. The MLD evolution classes are defined based on the values of $\partial_t h/h$. The "strong deepening" class is defined by $\partial_t h/h \geq 10\,\%/$day, "deepening" by $1\,\%/$day $\leq \partial_t h/h < 10\,\%/$day, "stable" by $-1\,\%/$day $\leq \partial_t h/h < 1\,\%/$day and "restratification" by $\partial_t h/h < -1\,\%/$day. The class of a hexagon is the majority class of its constituent points. If this majority class represents less than $50\,\%$ of the constituent points, the hexagon is tagged "non-significant" (superimposed black hexagon), if it is between $50\,\%$ and $75\,\%$ it is "significant" (superimposed black dot) and if it is higher than $75\,\%$ it is "highly significant" (nothing superimposed). A grid representing the slope 2/3 isolines of R_h^* is added in the $\lambda_s > 0$ panel of the λ_s - R_h parameter space. Dashed lines highlight demarcations between MLD evolution regimes discussed in the text.

486 • **Horizontal thresholds and sloping lines in the zone $\lambda_s > 0$:** The demar-

487 cations remain horizontal for $\lambda_s < 0.2$. Beyond that, for $\lambda_s > 0.2$, demarcations

488 follow lines with a 2/3 slope, which are isolines of $R_h^* = (N_h h/w_*)^2$. In this zone

489 where $\lambda_s > 0.2$, only the value of the buoyancy-flux related Richardson number

490 R_h^* is important for predicting the MLD evolution regime. A value $R_h^* > 3000$

491 indicates a stable regime, while low values suggest deepening or strong deepen-

492 ing regimes. The fact that R_h^* is the important dimensionless number in the $\lambda_s >$

493 0.2 zone informs us that this zone is a buoyancy-flux-dominant zone ($G > P$).

494 To summarize the previous points, λ_s indicates a restratifying TKE-loss zone for

495 $\lambda_s < -3$ and a TKE-gain zone for $\lambda_s > -3$. The TKE-loss zone is buoyancy-

496 flux-dominant whereas the TKE-gain zone is either wind-dominant for $-3 < \lambda_s <$

497 0.2 and represented by demarcations by R_h, or buoyancy-flux-dominant for $\lambda_s >$

498 0.2 and represented by demarcations defined with R_h^*. For clarity, these interpre-

499 tations based on G and P are added on the top of Figure 2.a.

500 While the λ_s - R_h projection is the best 2D projection of the 3D parameter space,

501 we also explore the third dimension within this space. We sort the results according to

502 their f/N_h values and we plot different "slices" of the parameter space in Figure 3.

503 The influence of rotation, as assessed by the parameter f/N_h, appears to stabilize

504 the water column. To illustrate this effect, we highlight in Figure 3 the demarcations be-

505 tween the stable regime and the deepening regime. We also plot in Figure 4 the value

506 of these thresholds $R_{h,c}$ and $R_{h,c}^*$ as a function of f/N_h (normalized by their values $R_{h,c0}$

507 and $R_{h,c0}^*$ for $f/N_h \in [10^{-3.5}; 10^{-3.0}]$). The higher f/N_h, the lower are $R_{h,c}$ and $R_{h,c}^*$.

508 Consequently, in the presence of rotation, a weaker stratification and/or a higher forc-

509 ing (u^*/h or w^*/h) are required to achieve the same level of deepening as without ro-

510 tation. This reduced effective surface buoyancy/wind power input could be attributed

511 to the generation of inertial oscillations (Pollard et al., 1973) or by enhanced lateral buoy-

512 ancy flux (Boccaletti et al., 2007).

513 Rotation has a more pronounced effect on the wind forcing than the buoyancy forc-

514 ing because $R_{h,c}$ decreases more with f/N_h than $R_{h,c}^*$ (cf Figure 4). Hence, the region

515 for which the MLD deepening is driven by the wind narrows with f/N_h compared to the

516 region for which the MLD deepening is driven by the surface buoyancy forcing. The $\lambda_{s,c}$

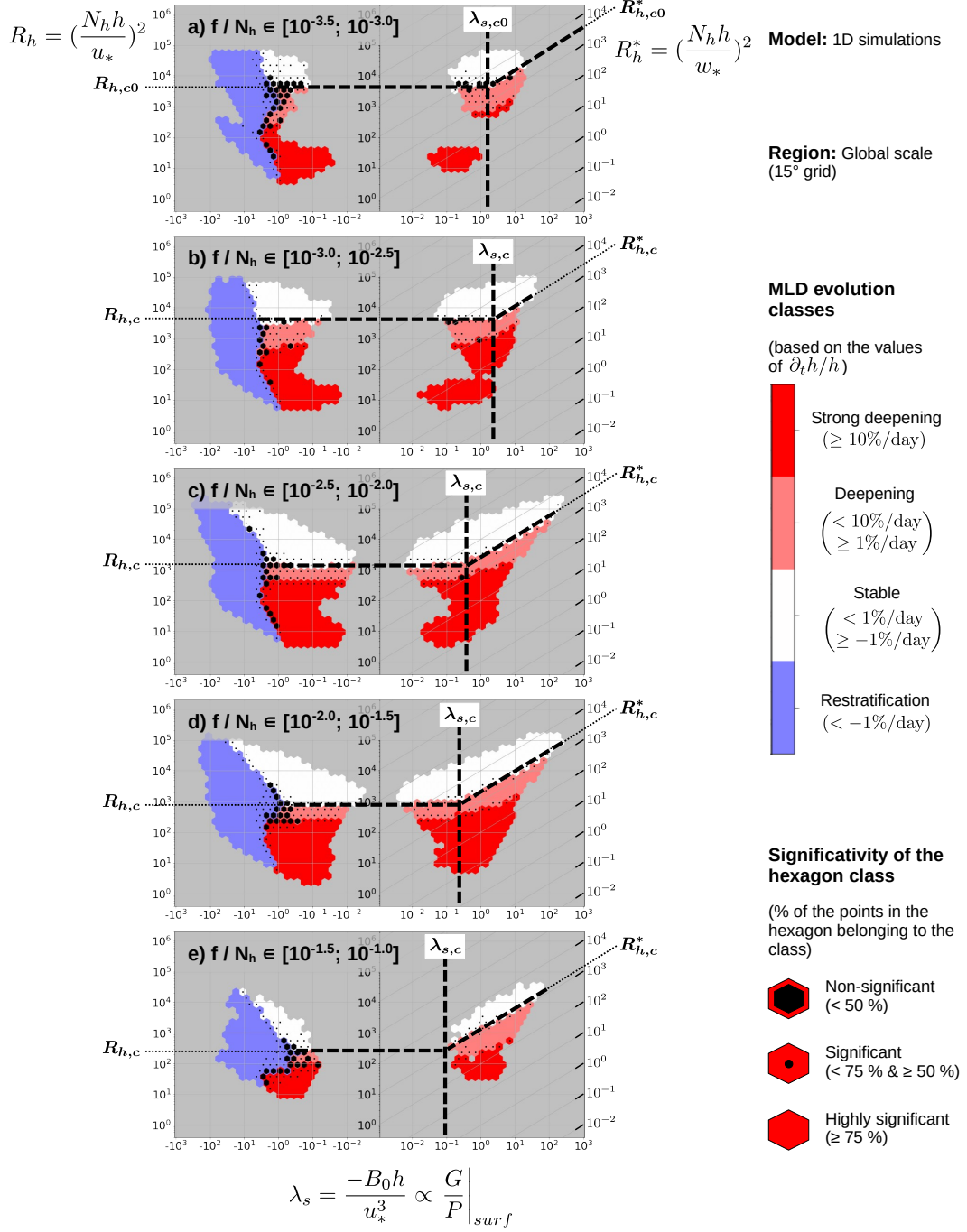517 thresholds that delineate these two regions are plotted in Figure 3 and their correspond-

Figure 3. Results of the 1D simulations performed at the locations of the 15° global grid plotted in the λ_s - R_h parameter space. The results are filtered according to their f/N_h values: (a) $f/N_h \in [10^{-3.5}; 10^{-3.0}]$, (b) $f/N_h \in [10^{-3.0}; 10^{-2.5}]$, (c) $f/N_h \in [10^{-2.5}; 10^{-2.0}]$, (d) $f/N_h \in [10^{-2.0}; 10^{-1.5}]$ and (e) $f/N_h \in [10^{-1.5}; 10^{-1.0}]$. Dashed lines highlight the thresholds $R_{h,c}$ and $R_{h,c}^*$ between the stable and the deepening regimes, and $\lambda_{s,c}$ the limit between the wind-dominant and the surface-buoyancy-flux-dominant zones. Values $R_{h,c0}$, $R_{h,c0}^*$ and $\lambda_{s,c0}$ are the ones for $f/N_h \in [10^{-3.5}; 10^{-3.0}]$. Other graphical conventions as in Figure 2.
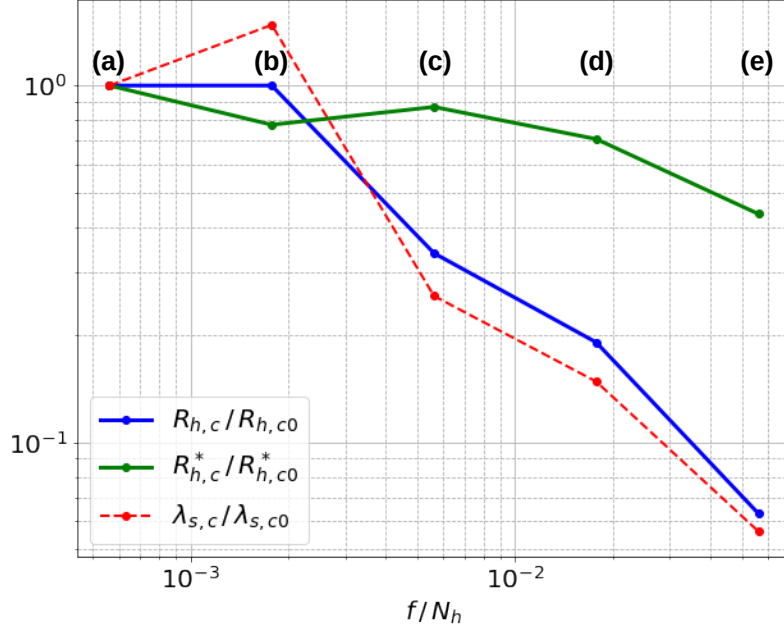
Figure 4. Dependence on f/N_h of the three demarcation thresholds $R_{h,c}$, $R_{h,c}^*$ and $\lambda_{s,c}$. The thresholds $R_{h,c}$ and $R_{h,c}^*$ indicate the demarcation between the stable and the deepening regimes respectively in the wind-dominant zone and in the surface-buoyancy-forcing-dominant zone. The threshold $\lambda_{s,c} = (R_{h,c}/R_{h,c}^*)^{3/2}$ indicates the transition between these wind-dominant zone and surface-buoyancy-forcing-dominant zone. These three thresholds are plotted normalized by their values at the lowest f/N_h: $R_{h,c0}$, $R_{h,c0}^*$ and $\lambda_{s,c0}$. Letters (a), (b), (c), (d), and (e) refer to the subfigures of Figure 3.
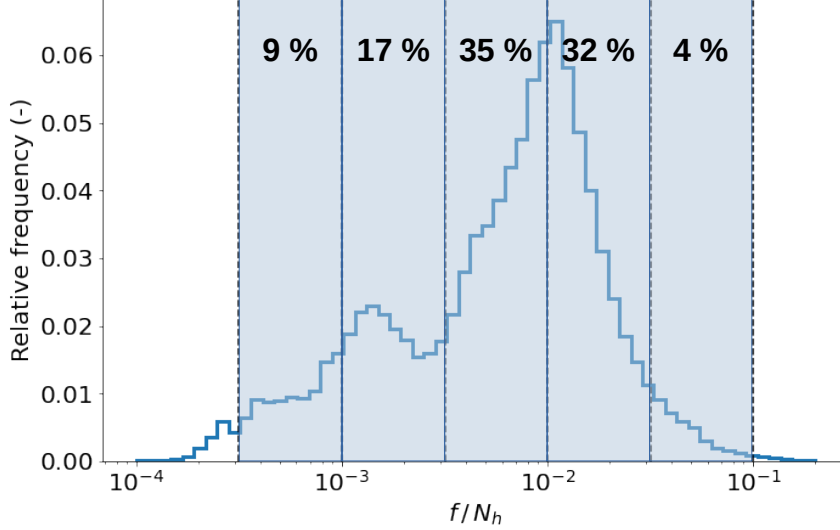
Figure 5. Relative frequency of the values of f/N_h for the 1D simulations at the global scale. The five slices used in Figure 3 are highlighted in light blue and the percentages of values falling in each of them are given.

ing values are reported in Figure 4 (following Equation 10, it could be calculated by $\lambda_{s,c} = (R_{h,c}/R_{h,c}^*)^{3/2}$). This dependency on f/N_h suggests that regions near the Equator are more likely to be in the wind-dominant regime, whereas high-latitude regions are more inclined toward a buoyancy-dominant regime.

As previously observed, the λ_s - R_h parameter space (Figure 2.a) exhibits high levels of significance even if the dimension f/N_h is not considered. This suggests that variations of the f/N_h parameter are less important than variations of λ_s and R_h for predicting a MLD evolution regime. Compared to the influence of f/N_h observed in Figure 3, this behavior can be explained by the fact that the f/N_h distribution of the 1D simulations at the global scale is not uniform but dominated by values of $f/N_h \in [10^{-2.5}; 10^{-1.5}]$ (cf Figure 5; and one can indeed see that demarcations of the Figure 2.a are close to the demarcations in Figure 3.c and Figure 3.d). Given the high statistical performance of the λ_s - R_h parameter space, and because it is easier to work in two dimensions, we will focus solely on the λ_s - R_h projection in the remainder of this article. The dimension f/N_h will only be considered if necessary to comprehend low significance levels.

We conclude this section by noting that the statistical performance of the parameter space is not specific to the TKE vertical mixing scheme (see Appendix A for a brief

presentation of results with the KPP scheme). Additionally, for informative purposes, the density maps and associated joint Probability Density Functions (PDF) showing the density distribution of the values of λ_s, R_h, and f/N_h in the three 2D projections of the 3D parameter space are given in Appendix B. This information can be useful when selecting relevant values of forcing and preconditioning conditions (u_*, B_0, N_h) in the context of parameter tuning (Souza et al., 2020; Wagner et al., 2023).

3.2 Influence of the Horizontal Resolution on the MLD Evolution Regimes for 3D Ocean Circulation Models

Figure 6 displays the results of the 1D simulations, eORCA1, eORCA12, and eNATL60 in the λ_s - R_h parameter space for the global scale and in the Western Mediterranean region. Since all four simulations used the same 1D vertical scheme TKE+EVD, any variations between the figures are attributed to the influence of lateral processes.

At the global scale, the main demarcation lines are consistent across the three simulations. This observation suggests that, for predicting the MLD evolution, lateral processes are of second importance in comparison with the 1D processes presented via λ_s and R_h. However, this observation may not be locally valid. Extractions of the three same simulations in the Western Mediterranean, in addition to the eNATL60 simulation (which could not be considered at the global scale due to its basin-scale nature), reveal significant variations across different resolutions. This indicates that the lateral processes play a substantial role in this region and cannot be neglected when compared to the 1D processes. Further details on these changes are provided in the following four paragraphs.

For $\lambda_s > -3$ and high values $R_h > 4000$ and $R_h^* > 4000$, the high resolution simulations (1/12° and 1/60°) exhibit some restratification points. High values of R_h and R_h^* indicate a stable MLD in terms of the 1D processes. The presence of restratification points suggests that the lateral processes, such as restratification by baroclinic instability at convective fronts or at mesoscale eddy fronts can become dominant and result in a MLD shoaling. In the same conditions ($\lambda_s > -3$; $R_h > 4000$; $R_h^* > 4000$), the 1° model behaves similarly to the 1D simulations, exhibiting a "stable" regime. This suggests that the coarse-resolution 1° model poorly resolves lateral processes of restratification.
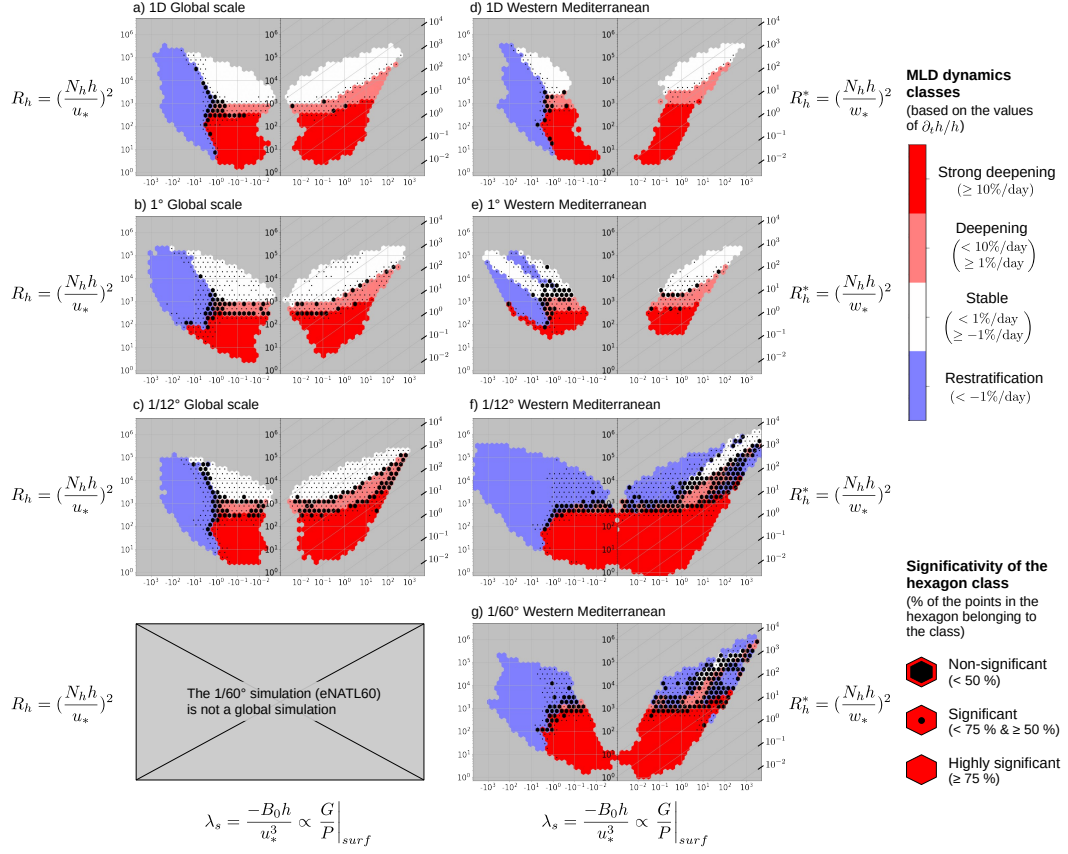
Figure 6. Results in the λ_s - R_h parameter space of the (a) 1D, (b) 1° eORCA1 and (c) 1/12° eORCA12 simulations at the global scale; and of the (d) 1D, (e) 1° eORCA1, (f) 1/12° eORCA12 and (g) 1/60° eNATL60 simulations for the Western Mediterranean region. Graphical conventions as in Figure 2.

For $\lambda_s > -3$ and low $R_h < 400$, going from 1D to 3D does not have a significant impact: the "strong deepening" regime is maintained in all four simulations. Low values of R_h indicate an unstable water column where the stratification is low compared to the wind forcing. The preservation of the "strong deepening" regime in all simulations suggests that for $R_h < 400$ the lateral processes of restratification cannot neutralize this instability and, therefore, play a secondary role.

The zone with $\lambda_s < -3$, dominated by surface buoyancy fluxes is a zone of restratification or stable regimes for the 1D simulations. As mentioned earlier, we associated this behavior with a TKE-loss in the 1D TKE budget. Interestingly, this $\lambda_s < -3$ zone characterized by restratification or stable regimes is still observed in the 3D models. This implies that for a dominant surface-buoyancy restratifying flux ($\lambda_s < -3$), the lateral processes of TKE generation (such as an Ekman flow creating an equivalent destabilizing wind-driven buoyancy flux, see for example Thomas & Lee, 2005) are of secondary importance compared to the processes of the 1D TKE budget.

The percentage of significant hexagons decreases when increasing the resolution: it is 97% in 1D, 88% at 1°, 84% at 1/12° and 78% at 1/60°. Non-significant hexagons indicate that the predictive skill of the parameter space for the MLD evolution is hampered by the importance of lateral processes. Considering the parameter f/N_h does not improve the results (not shown). Other parameters, some of which are described in section 2.2, could improve the predictability. Investigating these higher-dimensional parameter spaces could be a focus for future research.

3.3 Impact of the GM Parameterization on a 1° Coarse-resolution Model

In Figure 7, we plot the results of the eORCA1, eORCA1GM, and eNATL60 simulations in the Western Mediterranean and the Labrador regions separately. We recall that eORCA1GM differs from eORCA1 solely due to the addition of the GM parameterization, designed to represent the adiabatic advective effect of unresolved mesoscale processes (Gent, 2011). Using eNATL60 as a reference helps evaluate how these mesoscale processes can influence the MLD evolution regimes in the parameter space. Therefore, comparing eORCA1GM and eNATL60 provides valuable insights into the impact of the GM parameterization, even though the GM parameterization was not designed to tackle the impact of the mesoscale processes in the mixed layer.

The impact of the GM parameterization is minimal in the Western Mediterranean region (Figure 7.a and Figure 7.b), although resolving the mesoscale processes was for instance expected to change the MLD evolution regimes from "stable" to "restratification" at high $R_h > 2000$ and high $R_h^* > 2000$ (Figure 7.a and Figure 7.c).

In the Labrador region, the GM parameterization has a visible impact where its main contribution is to generate a restratification zone at middle stability conditions ($200 < R_h < 2000$ in $-3 < \lambda_s < 2$; $200 < R_h^* < 2000$ in $\lambda_s > 2$) whereas it was before mainly a deepening zone (Figure 7.d and Figure 7.e). However, neither the stable zone ($R_h > 2000$ in $-3 < \lambda_s < 2$; $R_h^* > 2000$ in $\lambda_s > 2$) nor the strong deepening zone ($R_h < 200$ in $-3 < \lambda_s < 2$; $R_h^* < 200$ in $\lambda_s > 2$) are affected. These changes are not comparable with the effect of the mesoscale processes represented by the $1/60°$ results (comparison Figure 7.d and Figure 7.f) for which, for instance, the restratification zone at middle stability conditions ($200 < R_h < 2000$ in $-3 < \lambda_s < 2$; $200 < R_h^* < 2000$ in $\lambda_s > 2$) is not observed.

Therefore, these two cases highlight that the impact of the mesoscale processes on the MLD evolution is not adequately captured by GM. To better characterize the impact of the GM parameterization as a function of the position in the parameter space, we can examine a proxy for its activation. The GM parameterization tends to flatten isopycnals by advecting tracers via eddy-induced velocities (Gent et al., 1995)

$$
\begin{aligned}
u_{GM} &= -\partial_z(\kappa_{GM} S_x) \\
v_{GM} &= -\partial_z(\kappa_{GM} S_y) \\
w_{GM} &= \partial_x(\kappa_{GM} S_x) + \partial_y(\kappa_{GM} S_y)
\end{aligned}
\tag{12}
$$

with κ_{GM} the isopycnal thickness diffusivity, $S_x = -\partial_x\rho/\partial_z\rho$ the zonal isopycnal slope and $S_y = -\partial_y\rho/\partial_z\rho$ the meridional isopycnal slope.

We construct an index to quantify the magnitude of the GM rectification by considering the horizontal transports integrated over the mixed layer $\gamma_x = \int_{-h}^0 -\partial_z(\kappa_{GM} S_x)dz$ and $\gamma_y = \int_{-h}^0 -\partial_z(\kappa_{GM} S_y)\, dz$. The surface boundary condition imposes $w_{GM} = 0$. This condition is often satisfied by taking $\kappa_{GM} S_x = \kappa_{GM} S_y = 0$ at the surface. Thus $\gamma_x = \kappa_{GM}(z = -h)S_x(z = -h)$ and $\gamma_y = \kappa_{GM}(z = -h)S_y(z = -h)$: the integrated horizontal transports are proportional to the isopycnal slopes at the mixed layer base. The index is then constructed as the maximal isopycnal slope over the x and the y axes
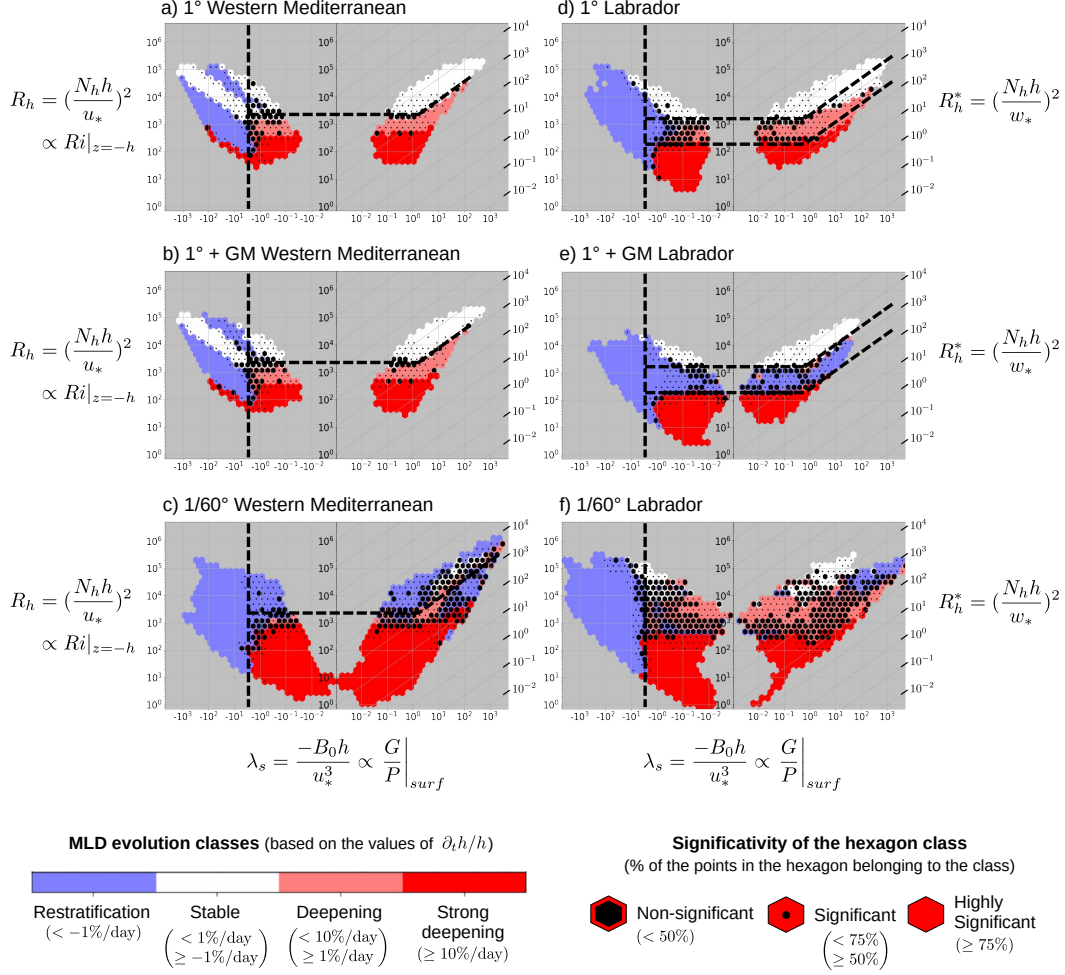
Figure 7. Results in the Western Mediterranean region of the (a) eORCA1, (b) eORCA1GM, and (c) eNATL60 simulations in the λ_s - R_h parameter space. Figures (d), (e), and (f) are the same in the Labrador region. Dashed lines highlight important demarcations discussed in the text. Graphical conventions as in Figure 2.

$$S_h = \max\left(|S_x\left(z=-h\right)|; \, |S_y\left(z=-h\right)|\right)$$
$$= \max\left(|\frac{\partial_x\,\rho\left(z=-h\right)}{\partial_z\rho\left(z=-h\right)}|; \, |\frac{\partial_y\,\rho\left(z=-h\right)}{\partial_z\rho\left(z=-h\right)}|\right) \tag{13}$$

with $\partial_z\rho(z=-h)$ calculated over a distance $0.1h$ below the mixed layer: $\partial_z\rho\left(z=-h\right) = \frac{\rho(z=-1.1h)-\rho(z=-h)}{0.1h}$.

The regions where the GM parameterization has a notable impact are characterized by high values of S_h (Figure 8.a and Figure 8.e; see also the comparison between Figures 8.b and 8.d, and Figures 8.f and 8.h). In the Western Mediterranean region, we can define a threshold $S_h = 0.5\,\mathrm{m/km}$ below which the GM parameterization is expected to have negligible impact. Filtering the eORCA1GM results by the condition $S_h < 0.5\,\mathrm{m/km}$, yields results comparable to the results of the eORCA1 simulation (comparison Figures 8.c and 8.d, and Figures 8.g and 8.h). This confirms that the observed impacts of the GM parameterization can be understood through the values of S_h. Hence, this number is an additional dimensionless number that could be considered when R_h and λ_s alone do not provide robust predictions. In future studies, exploring projections into parameter spaces $(\lambda_s,\, S_h)$ or $(R_h,\, S_h)$ could be promising avenues.

4 Conclusions and Discussion

This study introduces a three-dimensional parameter space designed to facilitate the analysis and the intercomparison of the ocean MLD evolution between numerical models. The parameter space consists of three dimensionless numbers R_h, λ_s and f/N_h derived through dimensional analysis: λ_s evaluates the relative influence of the buoyancy forcing and the wind forcing for producing/destroying TKE in the surface layer, R_h is the Richardson number describing the competition between the stabilizing effect of the pycnocline stratification and the destabilizing impact of the wind-induced shear. Finally, f/N_h evaluates the influence of the Earth's rotation.

The λ_s - R_h - f/N_h parameter space was first evaluated in the context of 1D simulations. Four MLD evolution regimes were defined based on the value of the relative MLD change $\partial_t h/h$: "Restratification", "Stable", "Deepening" and "Strong Deepening". We showed that the influence of rotation tends to stabilize the water column by reducing the effective forcings of the wind and the surface buoyancy flux. This reduction is even more pronounced on the wind forcing and consequently, MLD deepening in high
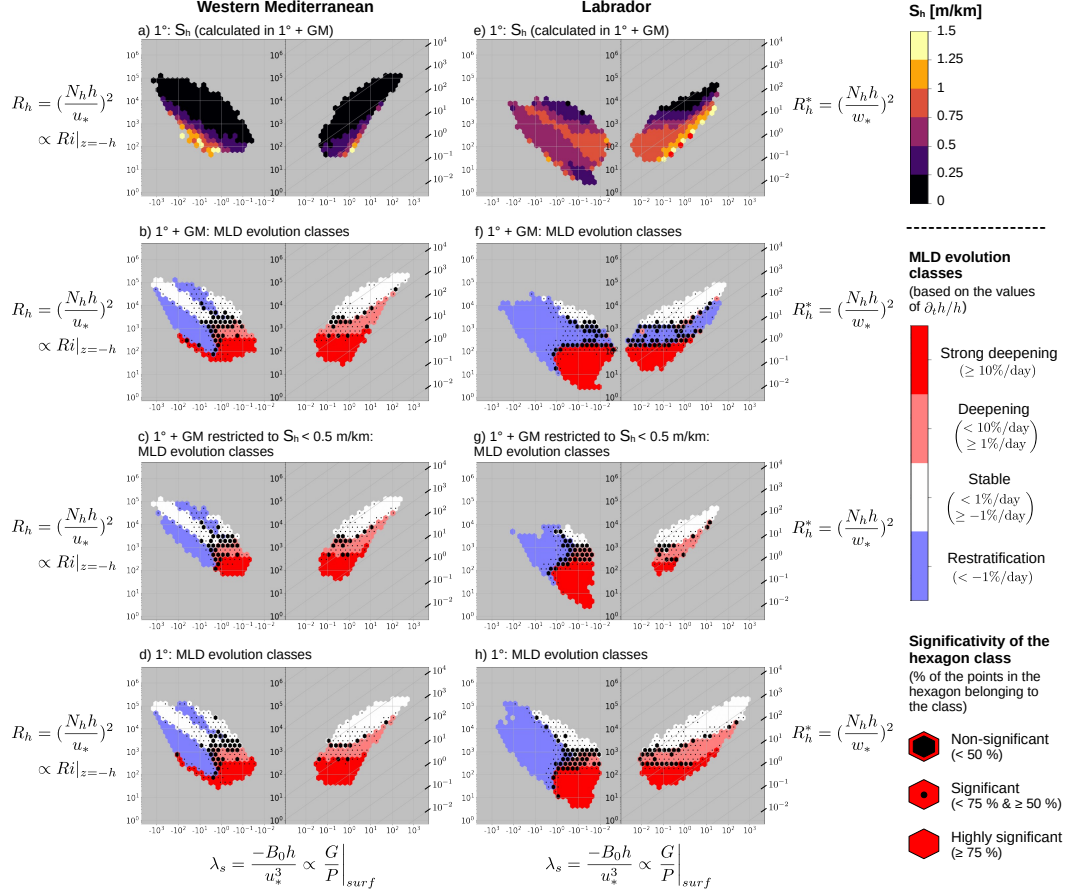
Figure 8. Results in the Western Mediterranean region in the λ_s - R_h parameter space of (a) S_h in eORCA1, (b) MLD evolution classes in eORCA1GM, (c) MLD evolution classes in eORCA1GM restricted to $S_h < 0.5$ m/km and (d) MLD evolution classes in eORCA1. Figures (d), (e), and (f) are the same in the Labrador region. The slope S_h of the isopycnes at the MLD is expressed in m/km. Values that exceeded 1.5 m/km are represented in red. Graphical conventions as in Figure 2.

latitude regions is more inclined to be dominated by the surface buoyancy forcing whereas the Equator is more inclined to be wind-dominant. This can be related to the numerous studies that assess the relative importance of wind and surface buoyancy forcings in different regions (Dong et al., 2007; Sallée et al., 2010; Downes et al., 2011; Holte et al., 2012; Sallée et al., 2021; Gao et al., 2023). For example, Sallée et al. (2010) stated that the surface buoyancy forcing in the Southern Ocean (high latitude) dominates the wind forcing by one order of magnitude. Our study, which shows the dependence on f/N_h of the $\lambda_{s,c}$ threshold between the two regimes, provides a new practical way of determining the relative importance of surface buoyancy flux versus wind.

The influence of the f/N_h parameter is less important than the λ_s and R_h parameters for predicting the MLD evolution. The two-dimensional parameter space λ_s - R_h indeed exhibits high statistical performances with, in 96 % of the cases, a pair (λ_s, R_h) that corresponds to a unique MLD evolution regime. In other words, instead of examining all the preconditioning and forcing conditions, one can just calculate the two dimensionless numbers λ_s and R_h for predicting the MLD evolution regimes. Also, the MLD evolution regimes appear in well-separated zones. This spatial coherence of regimes in this parameter space allows us to define thresholds on (λ_s, R_h) to predict MLD evolution regimes.

The thresholds of the λ_s - R_h parameter space were described in the context of 1D simulations. The criterion $\lambda_s < -3$ indicates stable or restratification regimes and is valid for all f/N_h values. The wind-dominant zone $-3 < \lambda_s < 0.2$ is characterized by transitions according to R_h-only thresholds. In the buoyancy-flux-dominant zone $\lambda_s > 0.2$, transitions between regimes can be seen as thresholds on $R_h^* = (N_h h/w_*)^2$, the Richardson number associated with the destabilizing buoyancy flux. This threshold at $\lambda_s \approx 0.2$ between the wind-dominant and the surface-buoyancy-flux-dominant zones is the one for the global scale, which is representative of f/N_h values in $[10^{-2.5}; 10^{-1.5}]$, and must be adjusted for different values of f/N_h.

Two applications of the parameter space were presented and we show how it may be used with realistic ocean models. In the first application, we intercompare ocean simulations at different horizontal resolutions to evaluate the effect of lateral processes on the MLD evolution. We showed that lateral processes play a secondary role for low values of R_h and R_h^*: the stratification effect is weak compared to the forcing u_* or w_* and

the "strong deepening" regime can be predicted without considering lateral processes. When the water column is stable with respect to 1D processes (large values of R_h and R_h^*), we showed that the lateral restratification processes become dominant in the high-resolution simulations (1/12° and 1/60°). These lateral processes may for example include the restratification by baroclinic instability at convective fronts or at mesoscale eddy fronts. However, the 1° model behaves as the 1D model, suggesting that the lateral processes of restratification are not resolved at this resolution without GM. Finally, in the high-resolution simulations (1/12° and 1/60°), the non-significant zones at mid values of R_h and R_h^* indicate that the lateral processes are dominant and that other dimensionless numbers could be considered for predicting the MLD evolution regime.

The second application shows that the adiabatic advective effect of the mesoscale processes parameterized by GM parameterization does not capture the full impact of unresolved mesoscale processes on the MLD evolution regimes in a coarse-resolution 1° model. In this context, we introduced the dimensionless number S_h which is the maximal isopycnal slope at the mixed layer base. This slope is one of the other dimensionless numbers that could be considered when the two (R_h, λ_s) are not sufficient for obtaining robust predictions. Particularly, projections into the parameter space (λ_s, S_h) or (R_h, S_h) could constitute some developments for future works.

The two applications presented in this study are not exhaustive. We decided to focus here on the use of the parameter space for model sensitivity studies. Future work could use the parameter space for comparing the behaviors of different vertical mixing schemes (KPP, TKE, GLS) and for comparing coupled and forced models. The information of the joint PDF of the three 2D projections of the 3D parameter space, given in Appendix B could also be used for choosing relevant values of forcing and preconditioning conditions (u_*, B_0, N_h) in the context of parameter tuning (Souza et al., 2020; Wagner et al., 2023). Beyond these direct applications, an interesting extension of the approach would be to evaluate the performance of the parameter space with LES data and observations. For the observations, ARGO floats could for example be used. They give profiles over 10-day periods and the parameter space will need to be assessed with this new period. Fluxes between the ocean and the atmosphere could for example be obtained through the European Centre for Medium-Range Weather Forecasts (ECMWF) open data. For the LES, it would be possible to keep the 1-day period developed in this study or to try also with shorter or longer periods. In short, if the statistical performance

is still obtained in these contexts, the parameter space could become an informative tool for calibrating the mixing schemes using LES or observational data as a truth.

Appendix A   Analysis with the KPP Vertical Mixing Scheme

To verify if the statistical performance of the parameter space is sensitive to the vertical mixing scheme, we performed the same collection of 1D water column simulations described in section 2.7 but with a KPP scheme instead of a TKE + EVD scheme. Figure A1 presents the results of these simulations with the same conventions as Figure 2. Again, the λ_s - N_h parameter space performs well with 96% of significant hexagons, and spatial coherence of well-delimited zones is still obtained. The demarcation thresholds (represented by dashed lines) could again be discussed. In short, all the diagnostics we have done previously could have been done with simulations based on the KPP scheme as well, and future research could focus on analyzing the difference in behaviors between the TKE + EVD scheme and the KPP mixing scheme.

Appendix B   Joint PDF of Three 2D Projections of the 3D Parameter Space

We plot in Figure B1 the density maps in the three 2D projections of the 3D parameter space and the contours of the associated joint PDF, calculated with the 1D simulations outputs at the global scale through the Python functions provided by Q. Li et al. (2019). These contours enclose 30% (black), 60% (blue), 90% (green), and 99% (yellow) of all instances centered at the highest PDF.

Appendix C   Open Research

All the codes used for the study are available through the following GitHub repository: `https://github.com/legaya/James2023_ParameterSpace/`. It contains the Jupyter Notebook used for performing the 1D simulations and all the analyses, the 1D model described in section 2.1 as a Fortran Module "scm_oce.so", and the Fortran codes needed for generating this module. The eORCA1, eORCA1GM, eORCA12, and eNATL60 simulations outputs needed for realizing the figures are available as netCDF files and "npz" archives via the following DOI: `https://doi.org/10.5281/zenodo.10423178`.
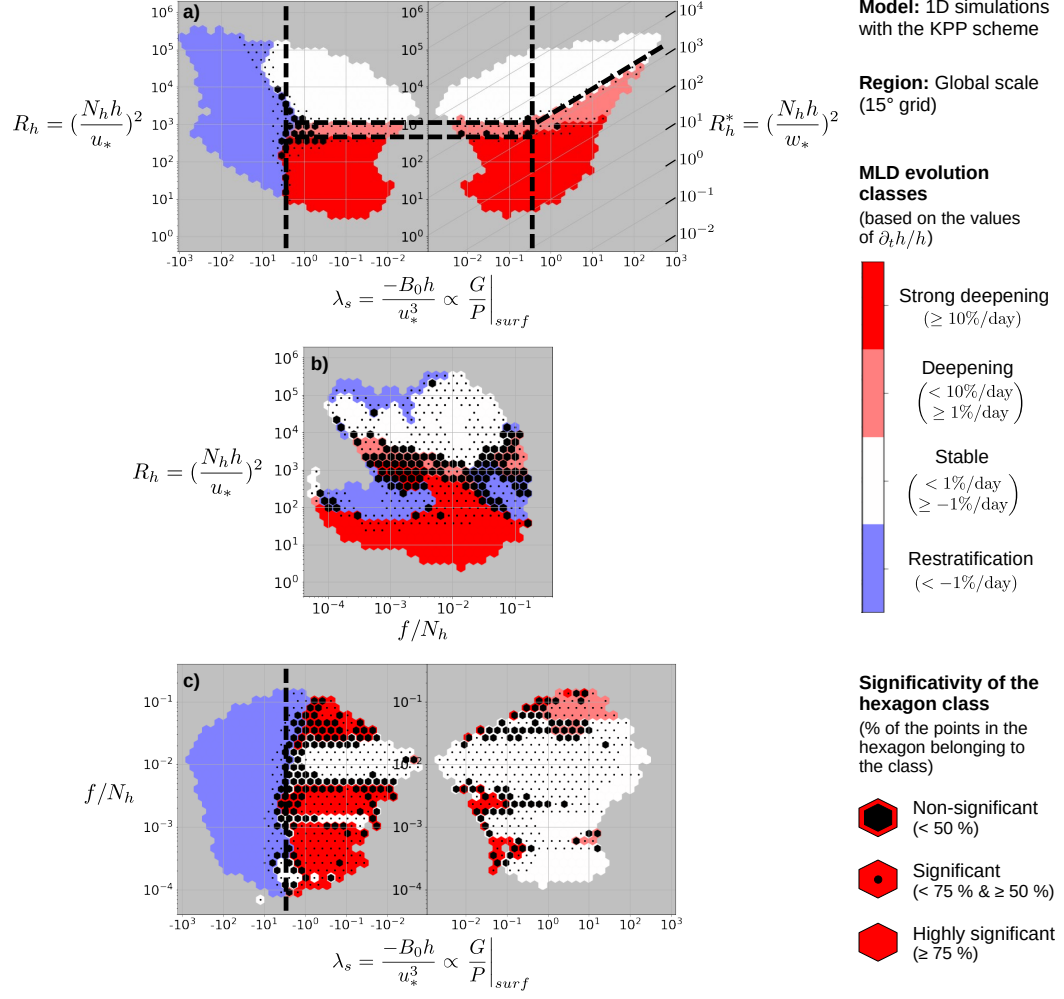
Figure A1. Same as Figure 2 but with 1D simulations using a KPP vertical mixing scheme instead of a TKE + EVD scheme.
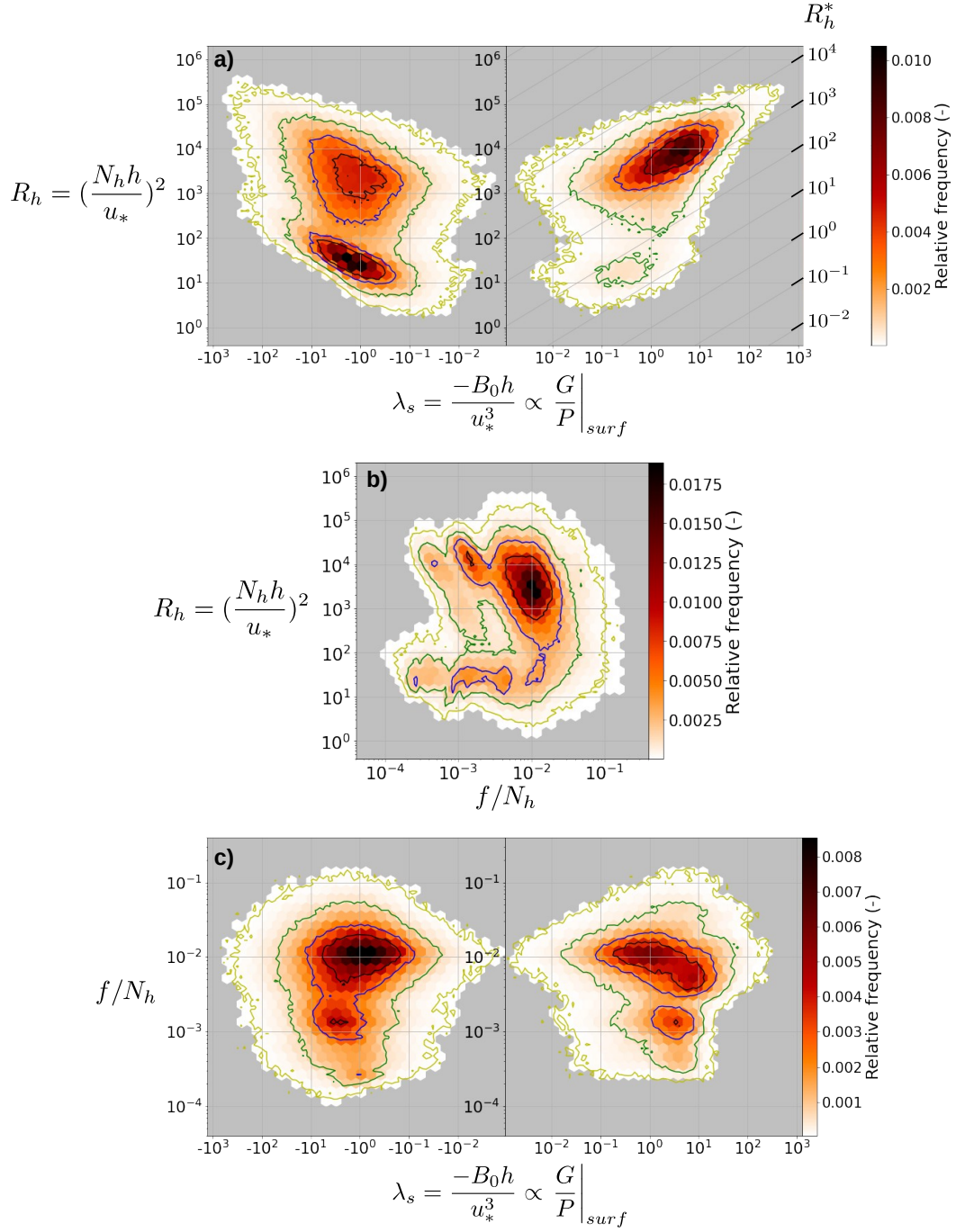
Figure B1. Density maps of the 1D simulations at the global scale for the a) λ_s - R_h, b) f/N_h - R_h and c) λ_s - f/N_h parameter space. The contours of the associated joint PDF are superimposed. These contours enclose 30% (black), 60% (blue), 90% (green), and 99% (yellow) of all instances centered at the highest PDF.

Acknowledgments

References

Aurnou, J. M., Horn, S., & Julien, K. (2020). Connections between nonrotating, slowly rotating, and rapidly rotating turbulent convection transport scalings. *Phys. Rev. Ress.*, *2*(4), 043115. doi: 10.1103/PhysRevResearch.2.043115

Banks, H. T., & Gregory, J. M. (2006). Mechanisms of ocean heat uptake in a coupled climate model and the implications for tracer based predictions of ocean heat uptake. *Geophysical Research Letters*, *33*(7), L07608. doi: 10.1029/2005GL025352

Belcher, S. E., Grant, A. L. M., Hanley, K. E., Fox-Kemper, B., Van Roekel, L., Sullivan, P. P., . . . Polton, J. A. (2012). A global perspective on Langmuir turbulence in the ocean surface boundary layer: FRONTIER. *Geophysical Research Letters*, *39*(18). doi: 10.1029/2012GL052932

Bernardello, R., Marinov, I., Palter, J. B., Galbraith, E. D., & Sarmiento, J. L. (2014). Impact of Weddell Sea deep convection on natural and anthropogenic carbon in a climate model. *Geophysical Research Letters*, *41*(20), 7262–7269. doi: 10.1002/2014GL061313

Boccaletti, G., Ferrari, R., & Fox-Kemper, B. (2007). Mixed Layer Instabilities and Restratification. *Journal of Physical Oceanography*, *37*(9), 2228–2250. doi: 10 .1175/JPO3101.1

Bouillaut, V., Lepot, S., Aumaître, S., & Gallet, B. (2019). Transition to the ultimate regime in a radiatively driven convection experiment. *J. Fluid Mech.*, *861*, R5. doi: 10.1017/jfm.2018.972

Brodeau, L., Le Sommer, J., & Albert, A. (2020). *ocean-next/eNATL60: Material*

describing the set-up and the assessment of NEMO-eNATL60 simulations. Zenodo. doi: 10.5281/ZENODO.4032732

Burchard, H., & Bolding, K. (2001). Comparative Analysis of Four Second-Moment Turbulence Closure Models for the Oceanic Mixed Layer. *Journal of Physical Oceanography*, *31*(8), 1943–1968. doi: 10.1175/1520-0485(2001)031⟨1943: CAOFSM⟩2.0.CO;2

Damerell, G. M., Heywood, K. J., Calvert, D., Grant, A. L., Bell, M. J., & Belcher, S. E. (2020). A comparison of five surface mixed layer models with a year of observations in the North Atlantic. *Progress in Oceanography*, *187*, 102316. doi: 10.1016/j.pocean.2020.102316

de Boyer Montégut, C., Madec, G., Fischer, A. S., Lazar, A., & Iudicone, D. (2004). Mixed layer depth over the global ocean: An examination of profile data and a profile-based climatology. *Journal of Geophysical Research*, *109*(C12), C12003. doi: 10.1029/2004JC002378

Dee, D. P., Uppala, S. M., Simmons, A. J., Berrisford, P., Poli, P., Kobayashi, S., ... Vitart, F. (2011). The ERA-Interim reanalysis: configuration and performance of the data assimilation system. *Quarterly Journal of the Royal Meteorological Society*, *137*(656), 553–597. doi: 10.1002/qj.828

Deremble, B. (2016). Convective plumes in rotating systems. *J. Fluid Mech.*, *799*, 27–55. doi: 10.1017/jfm.2016.348

Dong, S., Gille, S. T., & Sprintall, J. (2007). An Assessment of the Southern Ocean Mixed Layer Heat Budget. *Journal of Climate*, *20*(17), 4425–4442. doi: 10 .1175/JCLI4259.1

Downes, S. M., Budnick, A. S., Sarmiento, J. L., & Farneti, R. (2011). Impacts of wind stress on the Antarctic Circumpolar Current fronts and associated subduction: ACC FRONTS AND SUBDUCTION. *Geophysical Research Letters*, *38*(11), n/a–n/a. doi: 10.1029/2011GL047668

Ekman, V. W. (1905). On the influence of earth's rotation on ocean currents. *Ark. Math. Astron. Phys.*, *2*, 1–53.

Fearon, G., Herbette, S., Veitch, J., Cambon, G., Lucas, A. J., Lemarié, F., & Vichi, M. (2020). Enhanced vertical mixing in coastal upwelling systems driven by diurnal-inertial resonance: Numerical experiments. *Journal of Geophysical Research: Oceans*, *125*(9), e2020JC016208. doi: 10.1029/2020JC016208

Fofonoff, N. P., & Millard Jr, R. (1983). *Algorithms for the computation of funda-mental properties of seawater.* (Tech. Rep.). UNESCO. doi: 10.25607/OBP-1450

Fox-Kemper, B., Ferrari, R., & Hallberg, R. (2007). Parameterization of Mixed Layer Eddies. I: Theory and Diagnosis. *Journal of Physical Oceanography*. doi: 10.1175/2007JPO3792.1

Gao, Y., Kamenkovich, I., & Perlin, N. (2023). Origins of mesoscale mixed-layer depth variability in the Southern Ocean. *Ocean Science*, *19*(3), 615–627. doi: 10.5194/os-19-615-2023

Gaspar, P. (1988). Modeling the seasonal cycle of the upper ocean. *Journal of Physical Oceanography*, *18*(2), 161 - 180. doi: 10.1175/1520-0485(1988)018⟨0161: MTSCOT⟩2.0.CO;2

Gaspar, P., Grégoris, Y., & Lefevre, J.-M. (1990). A simple eddy kinetic energy model for simulations of the oceanic vertical mixing: Tests at station Papa and long-term upper ocean study site. *Journal of Geophysical Research*, *95*(C9), 16179. doi: 10.1029/JC095iC09p16179

Gent, P. R. (2011). The Gent–McWilliams parameterization: 20/20 hindsight. *Ocean Modelling*, *39*(1-2), 2–9. doi: 10.1016/j.ocemod.2010.08.002

Gent, P. R., & McWilliams, J. C. (1990). Isopycnal mixing in ocean circulation models. *Journal of Physical Oceanography*, *20*(1), 150 - 155. doi: 10.1175/1520-0485(1990)020⟨0150:IMIOCM⟩2.0.CO;2

Gent, P. R., Willebrand, J., McDougall, T. J., & McWilliams, J. C. (1995). Parameterizing Eddy-Induced Tracer Transports in Ocean Circulation Models. *Journal of Physical Oceanography*, *25*(4), 463–474. doi: 10.1175/1520-0485(1995) 025⟨0463:PEITTI⟩2.0.CO;2

Giordani, H., Bourdallé-Badie, R., & Madec, G. (2020). An Eddy-Diffusivity Mass-Flux Parameterization for Modeling Oceanic Convection. *Journal of Advances in Modeling Earth Systems*, *12*(9). doi: 10.1029/2020MS002078

Griffies, S. M., Danabasoglu, G., Durack, P. J., Adcroft, A. J., Balaji, V., Böning, C. W., ... Yeager, S. G. (2016). OMIP contribution to CMIP6: experimental and diagnosticprotocol for the physical component of the Ocean Model Intercomparison Project. *Geoscientific Model Development*, *9*(9), 3231–3296. doi: 10.5194/gmd-9-3231-2016

Gutjahr, O., Brüggemann, N., Haak, H., Jungclaus, J. H., Putrasahan, D. A., Lohmann, K., & von Storch, J.-S. (2021). Comparison of ocean vertical mixing schemes in the Max Planck Institute Earth System Model (MPI-ESM1.2). *Geoscientific Model Development*, *14*(5), 2317–2349. doi: 10.5194/gmd-14-2317-2021

Hanjalić, K., & Launder, B. E. (1972). A Reynolds stress model of turbulence and its application to thin shear flows. *Journal of Fluid Mechanics*, *52*(4), 609–638. doi: 10.1017/S002211207200268X

Heuzé, C. (2017). North Atlantic deep water formation and AMOC in CMIP5 models. *Ocean Science*, *13*(4), 609–622. doi: 10.5194/os-13-609-2017

Holte, J. W., Talley, L. D., Chereskin, T. K., & Sloyan, B. M. (2012). The role of air-sea fluxes in Subantarctic Mode Water formation. *Journal of Geophysical Research: Oceans*, *117*(C3), 2011JC007798. doi: 10.1029/2011JC007798

Koenigk, T., Fuentes-Franco, R., Meccia, V. L., Gutjahr, O., Jackson, L. C., New, A. L., ... Sein, D. V. (2021). Deep mixed ocean volume in the Labrador Sea in HighResMIP models. *Climate Dynamics*, *57*(7-8), 1895–1918. doi: 10.1007/s00382-021-05785-x

Kraus, E. B., & Turner, J. S. (1967). A one-dimensional model of the seasonal thermocline II. *The general theory and its consequences. Tellus*, *19*(1), 98–106. doi: 10.1111/j.2153-3490.1967.tb01462.x

Kuhlbrodt, T., Griesel, A., Montoya, M., Levermann, A., Hofmann, M., & Rahmstorf, S. (2007). On the driving processes of the Atlantic meridional overturning circulation. *Reviews of Geophysics*, *45*(2), RG2001. doi: 10.1029/2004RG000166

Large, W. G., McWilliams, J. C., & Doney, S. C. (1994). Oceanic vertical mixing: A review and a model with a nonlocal boundary layer parameterization. *Reviews of Geophysics*, *32*(4), 363. doi: 10.1029/94RG01872

Lazar, A., Madec, G., & Delecluse, P. (1999). The deep interior downwelling, the veronis effect, and mesoscale tracer transport parameterizations in an ogcm. *Journal of Physical Oceanography*, *29*(11), 2945 - 2961. doi: https://doi.org/10.1175/1520-0485(1999)029⟨2945:TDIDTV⟩2.0.CO;2

Lellouche, J.-M., Chassignet, E., Bourdallé-Badie, R., Garric, G., Melet, A., Drévillon, M., ... Le Traon, P.-Y. (2021). The Copernicus Global 1/12°

Oceanic and Sea Ice GLORYS12 Reanalysis. *Frontiers in Earth Science*, *9*, 698876. doi: 10.3389/feart.2021.698876

Li, M., & Garrett, C. (1993). Cell merging and the jet/downwelling ratio in Langmuir circulation. *Journal of Marine Research*, *51*(4), 737–769. doi: 10.1175/1520-0485(1997)027⟨0121:MLDDTL⟩2.0.CO;2

Li, Q., Reichl, B. G., Fox-Kemper, B., Adcroft, A. J., Belcher, S. E., Danabasoglu, G., . . . Zheng, Z. (2019). Comparing Ocean Surface Boundary Vertical Mixing Schemes Including Langmuir Turbulence. *Journal of Advances in Modeling Earth Systems*, *11*(11), 3545–3592. doi: 10.1029/2019MS001810

Lévy, M., Mémery, L., & Madec, G. (1998). The onset of a bloom after deep winter convection in the northwestern Mediterranean sea: mesoscale process study with a primitive equation model. *Journal of Marine Systems*, *16*(1-2), 7–21. doi: 10.1016/S0924-7963(97)00097-3

Mack, S. A., & Schoeberlein, H. C. (2004). Richardson Number and Ocean Mixing: Towed Chain Observations. *Journal of Physical Oceanography*, *34*(4), 736–754. doi: 10.1175/1520-0485(2004)034⟨0736:RNAOMT⟩2.0.CO;2

Madec, G., Bourdallé-Badie, R., Chanut, J., Clementi, E., Coward, A., Ethé, C., . . . Moulin, A. (2022). *NEMO ocean engine.* (Publisher: Zenodo Version Number: v4.2) doi: 10.5281/ZENODO.1464816

Marshall, J., & Schott, F. (1999). Open-ocean convection: Observations, theory, and models. *Reviews of geophysics*, *37*(1), 1–64. doi: 10.1029/98RG02739

Mellor, G. L. (1973). Analytic prediction of the properties of stratified planetary surface layers. *Journal of Atmospheric Sciences*, *30*(6), 1061 - 1069. doi: 10.1175/1520-0469(1973)030⟨1061:APOTPO⟩2.0.CO;2

Mellor, G. L., & Durbin, P. A. (1975). The structure and dynamics of the ocean surface mixed layer. *Journal of Physical Oceanography*, *5*, 718-728. doi: 10.1175/1520-0485(1975)005⟨0718:TSADOT⟩2.0.CO;2

Mellor, G. L., & Yamada, T. (1974). A hierarchy of turbulence closure models for planetary boundary layers. *Journal of Atmospheric Sciences*, *31*(7), 1791 - 1806. doi: 10.1175/1520-0469(1974)031⟨1791:AHOTCM⟩2.0.CO;2

Mellor, G. L., & Yamada, T. (1982). Development of a turbulence closure model for geophysical fluid problems. *Reviews of Geophysics*, *20*(4), 851. doi: 10.1029/RG020i004p00851

Obukhov, A. M. (1971). Turbulence in an atmosphere with a non-uniform temperature. *Boundary-Layer Meteorology*, *2*(1), 7–29. doi: 10.1007/BF00718085

Pollard, R. T., Rhines, P. B., & Thompson, R. O. R. Y. (1973). The deepening of the wind-mixed layer. *Geophysical Fluid Dynamics*, *4*(4), 381–404. doi: 10.1080/03091927208236105

Price, J. F. (1979). On the scaling of stress-driven entrainment experiments. *Journal of Fluid Mechanics*, *90*(3), 509–529. doi: 10.1017/S0022112079002366

Price, J. F., Weller, R. A., & Pinkel, R. (1986). Diurnal cycling: Observations and models of the upper ocean response to diurnal heating, cooling, and wind mixing. *Journal of Geophysical Research*, *91*(C7), 8411. doi: 10.1029/JC091iC07p08411

Reichl, B. G., & Hallberg, R. (2018). A simplified energetics based planetary boundary layer (ePBL) approach for ocean climate simulations. *Ocean Modelling*, *132*, 112–129. doi: 10.1016/j.ocemod.2018.10.004

Rodi, W. (1987). Examples of calculation methods for flow and mixing in stratified fluids. *Journal of Geophysical Research*, *92*(C5), 5305. doi: 10.1029/JC092iC05p05305

Sallée, J.-B., Pellichero, V., Akhoudas, C., Pauthenet, E., Vignes, L., Schmidtko, S., ... Kuusela, M. (2021). Summertime increases in upper-ocean stratification and mixed-layer depth. *Nature*, *591*(7851), 592–598. doi: 10.1038/s41586-021-03303-x

Sallée, J. B., Speer, K. G., & Rintoul, S. R. (2010). Zonally asymmetric response of the Southern Ocean mixed-layer depth to the Southern Annular Mode. *Nature Geoscience*, *3*(4), 273–279. doi: 10.1038/ngeo812

Schulzweida, U. (2023). *Cdo user guide.* Zenodo. doi: 10.5281/zenodo.10020800

Shy, S. (1995). Mixing dynamics of jet interaction with a sharp density interface. *Experimental Thermal and Fluid Science*, *10*(3), 355–369. doi: 10.1016/0894-1777(94)00095-P

Simpson, J. H., & Hunter, J. R. (1974). Fronts in the irish sea. *Nature*, *250*(5465), 404–406. doi: 10.1038/250404a0

Souza, A. N., Wagner, G. L., Ramadhan, A., Allen, B., Churavy, V., Schloss, J., ... Ferrari, R. (2020). Uncertainty Quantification of Ocean Parameterizations: Application to the K-Profile-Parameterization for Penetrative Con-

vection. *Journal of Advances in Modeling Earth Systems*, *12*(12). doi: 10.1029/2020MS002108

Speer, K. G., & Marshall, J. (1995). The growth of convective plumes at seafloor hot springs. *J. Mar. Res*, *53*(6), 1025–1057. doi: 10.1357/0022240953212972

Stull, R. B. (Ed.). (1988). *An Introduction to Boundary Layer Meteorology.* Dordrecht: Springer Netherlands. doi: 10.1007/978-94-009-3027-8

Sverdrup, H. (1953). On conditions for the vernal blooming of phytoplankton. *J. Cons. Int. Explor. Mer*, *18*(3), 287–295. doi: 10.1093/icesjms/18.3.287

Sérazin, G., Tréguier, A. M., & De Boyer Montégut, C. (2023). A seasonal climatology of the upper ocean pycnocline. *Frontiers in Marine Science*, *10*, 1120112. doi: 10.3389/fmars.2023.1120112

Taylor, J. R., & Ferrari, R. (2011). Shutdown of turbulent convection as a new criterion for the onset of spring phytoplankton blooms. *Limnology and Oceanography*, *56*(6), 2293–2307. doi: 10.4319/lo.2011.56.6.2293

Thangam, S., Abid, R., & Speziale, C. G. (1992). Application of a new K-tau model to near wall turbulent flows. *AIAA Journal*, *30*(2), 552–554. doi: 10.2514/3.10952

Thomas, L. N., & Lee, C. M. (2005). Intensification of Ocean Fronts by Down-Front Winds. *Journal of Physical Oceanography*, *35*(6), 1086–1102. doi: 10.1175/JPO2737.1

Treguier, A. M., De Boyer Montégut, C., Bozec, A., Chassignet, E. P., Fox-Kemper, B., McC. Hogg, A., . . . Yeager, S. (2023). The mixed-layer depth in the Ocean Model Intercomparison Project (OMIP): impact of resolving mesoscale eddies. *Geoscientific Model Development*, *16*(13), 3849–3872. doi: 10.5194/gmd-16-3849-2023

Tsujino, H., Urakawa, S., Nakano, H., Small, R. J., Kim, W. M., Yeager, S. G., . . . Yamazaki, D. (2018). JRA-55 based surface dataset for driving ocean–sea-ice models (JRA55-do). *Ocean Modelling*, *130*, 79–139. doi: 10.1016/j.ocemod.2018.07.002

Turner, J. S. (1973). *Buoyancy effects in fluids.* Cambridge University Press. doi: 10.1017/CBO9780511608827

Turner, J. S. (1986). Turbulent entrainment: the development of the entrainment assumption, and its application to geophysical flows. *Journal of Fluid Mechanics*,

173, 431–471. doi: 10.1017/S0022112086001222

Umlauf, L., & Burchard, H. (2003). A generic length-scale equation for geophysical turbulence models. *Journal of Marine Research*, 61(2), 235–265. doi: 10.1357/002224003322005087

Umlauf, L., & Burchard, H. (2005). Second-order turbulence closure models for geophysical boundary layers. A review of recent work. *Continental Shelf Research*, 25(7-8), 795–827. doi: 10.1016/j.csr.2004.08.004

Ushijima, Y., & Yoshikawa, Y. (2020). Mixed layer deepening due to wind-induced shear-driven turbulence and scaling of the deepening rate in the stratified ocean. *Ocean Dynamics*, 70(4), 505–512. doi: 10.1007/s10236-020-01344-w

Van Der Laan, M. P., Kelly, M., Floors, R., & Peña, A. (2020). Rossby number similarity of an atmospheric RANS model using limited-length-scale turbulence closures extended to unstable stratification. *Wind Energy Science*, 5(1), 355–374. doi: 10.5194/wes-5-355-2020

Van Roekel, L., Adcroft, A. J., Danabasoglu, G., Griffies, S. M., Kauffman, B., Large, W., . . . Schmidt, M. (2018). The KPP Boundary Layer Scheme for the Ocean: Revisiting Its Formulation and Benchmarking One-Dimensional Simulations Relative to LES. *Journal of Advances in Modeling Earth Systems*, 10(11), 2647–2685. doi: 10.1029/2018MS001336

Vreugdenhil, C. A., & Gayen, B. (2021). Ocean Convection. *Fluids*, 6(10), 360. doi: 10.3390/fluids6100360

Wagner, G. L., Hillier, A., Constantinou, N. C., Silvestri, S., Souza, A., Burns, K., . . . others (2023). Catke: a turbulent-kinetic-energy-based parameterization for ocean microturbulence with dynamic convective adjustment. *arXiv preprint arXiv:2306.13204*.

Weber, J. E. (1983). Steady wind- and wave-induced currents in the open ocean. *Journal of Physical Oceanography*, 13(3), 524 - 530. doi: https://doi.org/10.1175/1520-0485(1983)013⟨0524:SWAWIC⟩2.0.CO;2

Wilcox, D. C. (1988). Reassessment of the scale-determining equation for advanced turbulence models. *AIAA Journal*, 26(11), 1299–1310. doi: 10.2514/3.10041

Willis, G., & Deardorff, J. (1974). A laboratory model of the unstable planetary boundary layer. *Journal of Atmospheric Sciences*, 31(5), 1297–1307. doi: 10.1175/1520-0469(1974)031⟨1297:ALMOTU⟩2.0.CO;2

Wyngaard, J. C. (1973). On the surface-layer turbulence. In *Workshop on microme-teorology* (pp. 101–149).

Zeierman, S., & Wolfshtein, M. (1986). Turbulent time scale for turbulent-flow cal-culations. *AIAA Journal*, *24*(10), 1606–1610. doi: 10.2514/3.9490

Zheng, Z., Harcourt, R. R., & D'Asaro, E. A. (2021). Evaluating Monin–Obukhov Scaling in the Unstable Oceanic Surface Layer. *Journal of Physical Oceanogra-phy*, *51*(3), 911–930. doi: 10.1175/JPO-D-20-0201.1

Zhu, Y., Zhang, R.-H., & Sun, J. (2020). North Pacific Upper-Ocean Cold Temper-ature Biases in CMIP6 Simulations and the Role of Regional Vertical Mixing. *Journal of Climate*, *33*(17), 7523–7538. doi: 10.1175/JCLI-D-19-0654.1